ภาคผนวก

Sensors and Actuators B 181 (2013) 388–394

Contents lists available at SciVerse ScienceDirect

Sensors and Actuators B: Chemical

journal homepage: www.elsevier.com/locate/snb

rbon doped tungsten oxide nanorods NO_2 sensor prepared by glancing angle sputtering

atchawal Wongchoosuk[a], Anurat Wisitsoraat[b], Ditsayut Phokharatkul[b], Mati Horprathum[c], isorn Tuantranont[b], Teerakiat Kerdcharoen[d,e,*]

[a] *artment of Physics, Faculty of Science, Kasetsart University, Chatuchak, Bangkok 10900, Thailand*
[b] *oelectronics and MEMS Laboratory, National Electronics and Computer Technology Center, Klong Luang, Pathumthani 12120, Thailand*
[c] *ical Thin-Film Laboratory, National Electronics and Computer Technology Center, Pathumthani 12120, Thailand*
[d] *artment of Physics and Center of Nanoscience and Nanotechnology, Faculty of Science, Mahidol University, Bangkok 10400, Thailand*
[e] *NOTEC Center of Excellence at Mahidol University, National Nanotechnology Center, Pathumthani 12120, Thailand*

T I C L E I N F O

le history:
ived 30 August 2012
ived in revised form
ecember 2012
pted 14 January 2013
lable online 4 February 2013

ords:
) technique
il oxides gas sensor
gen dioxide
ped WO_3
operating temperature
rod

A B S T R A C T

Metal oxide semiconductor nanostructures offer potential advantages in sensing applications due to their large surface to volume ratio, lower electron recombination rate, and high stability. However, most methods produce nanostructures with random sizes, distribution and orientations, which are not reliable for practical applications because of poor reproducibility. In this work, homogeneous carbon-doped WO_3 nanorods are developed based on the glancing angle deposition (GLAD) technique using radio-frequency magnetron sputtering and investigated for NO_2 gas sensing application. The carbon doping is achieved by using acetylene gas as a carbon source. Characterization based on scanning electron microscopy, Auger electron spectroscopy and X-ray diffraction confirm the formation of uniform carbon-doped crystalline WO_3 nanorods. The gas-sensing results reveal that carbon-doped WO_3 nanorods sensor exhibits not only high response and selectivity to NO_2 (0.5–5 ppm) but also at low operating temperature (150 °C) compared with the undoped ones. The observed gas-sensing enhancement may be attributed to the increase of specific surface area and the decrease of activation energy by carbon doping.

ntroduction

Nanostructures such as nanowires, nanorods, nanotubes of al oxide semiconductor (MOS) materials have recently acted monumental interest in gas-sensing applications because heir excellent performances owing to their large surface to vol- e ratio, lower electron recombination rate and high stability. ong various MOS materials, tungsten trioxide (WO_3) is a highly mising candidate due to its fast response with high sensitivity ard NO_x [1–4], H_2S [5–8], C_2H_5OH [8,9], CO [10], NH_3 [10–14], [15] and H_2 [16]. Moreover, addition of some foreign atoms n as Pt, Pd, or Au [17–21] to WO_3 usually improves the sen- vity and selectivity to some particular gases. However, these itives are mostly expensive noble metals, which are not practi- for low-cost applications. Recently, carbon based dopants have n reported as promising low-cost alternatives. For instance, carbon nanotubes (CNTs) incorporation has been shown to be effective for improving sensitivity and selectivity toward H_2 of WO_3 thin film [22]. In another research, carbon doping provides considerable enhancement of toluene vapor sensitivity of WO_3 microtubes at low operating temperature [23].

WO_3 nanostructures have been fabricated based on a number of methods including thermal oxidization [24–26], spray pyrolysis [27], and chemical vapor deposition [28,29]. However, most methods produce nanostructures with random sizes, distribution and orientations, which are not reliable for practical applications because of poor reproducibility. Recently, some processes including e-beam lithography, nanolithography and template-growth techniques have been developed to realize well-ordered nanostructures. Nevertheless, they require either expensive instrumentation or complicated fabrication procedures. Simple and low cost methods for well-ordered nanostructure construction are more preferred in gas-sensing and other commercial applications.

Glancing angle deposition (GLAD) technique is a relatively new method for fabrication of well-ordered and sophisticated nanostructures i.e. nanorods, nanoblade and zigzag nanocolumns [30–33]. It is a modified physical vapor deposition process, in which substrate surface is rotated and tilted to an angle greater than 80° with respect to the normal of substrate surface or less than 10°

Corresponding author at: Department of Physics and Center of Nanoscience and technology, Faculty of Science, Mahidol University, Bangkok 10400, Thailand. +66 22 015 770; fax: +66 22 015 843.
E-mail addresses: teerakiat.ker@mahidol.ac.th, sctkc@mahidol.ac.th erdcharoen).

-4005/$ – see front matter © 2013 Elsevier B.V. All rights reserved.
//dx.doi.org/10.1016/j.snb.2013.01.066

with respect to the direction of vapor flux. The vapor molecules directed to the substrate will experience shadowing and limited surface diffusion condition leading to the formation of isolated nanostructures. With this technique, the shape, size and density of nanostructures can be well controlled by deposition parameters such as deposition angle, operating pressure, substrate temperature, deposition power, and so on. There have been few reports of WO_3 nanorods fabricated by the GLAD technique using DC magnetron sputtering [34–36]. However, there has been no report of carbon-doped WO_3 nanorods prepared by the GLAD technique using radio-frequency (RF) magnetron sputtering and its application in gas sensing. In this work, carbon-doped WO_3 nanorods is fabricated by GLAD technique using RF magnetron sputtering and investigated for NO_2 gas sensing application. In addition, its performances are comparatively studied with that of the undoped ones.

2. Experimental details

2.1. Fabrication of WO_3 nanorod-based gas sensors

WO_3 nanorod-based gas sensors were fabricated by the direct deposition of WO_3 nanostructures onto prefabricated interdigitated electrodes on alumina substrates. Interdigitated electrodes were used to reduce the resistance of WO_3 material. These electrodes were prepared by sputtering Cr (~50 nm) and Au (~300 nm) on alumina substrates with pre-patterned photoresist and lift-off process. The interdigitated Au electrodes have a sensing area of 5 mm × 5 mm and the interdigit spacing of 100 μm. In addition, WO_3 nanorods were also deposited on bare silicon substrates for structural characterization. Prior to deposition, silicon wafers and alumina substrates were pre-cleaned successively with acetone and isopropanol by ultrasonication, dried in nitrogen atmosphere and then loaded into the deposition chamber.

Carbon-doped and undoped WO_3 nanorods were deposited by variable angle RF magnetron sputtering system as schematically illustrated in Fig. 1. A 3-inch tungsten disc with 99.995% purity (K.J. Lesker) was used as the sputtering target. The distance from the target to substrate center and the substrate rotation were fixed at 7 cm and 60 rpm, respectively. The chamber was evacuated by mechanical and turbomolecular pumps (Pfeiffer Inc.) while the vacuum pressure was continuously monitored with Pirani and Penning pressure gauges. For undoped WO_3 nanorod deposition, W target was reactively sputtered in a mixture of 99.999% argon and 99.999% oxygen after a base pressure of 5.6×10^{-6} mbar. The flow rates of Ar and O_2 were controlled with a mass flow controllers (MKS Inc.) at 9.6 and 11.0 sccm, respectively. The plasma discharge was generated at a constant RF power of 200 W at a sputtering pressure of 5.0×10^{-3} mbar for 3 h. The substrate normal was positioned at an angle of 85° ($\alpha = 85°$) with the respect to the vapor incident flux (the vertical axis). For carbon doping, 99.99% acetylene (C_2H_2) as a carbon source was added at a flow rate of 1.1 sccm into the gas mixture and RF plasma was induced at a sputtering pressure of 6.0×10^{-3} mbar. The undoped and carbon-doped WO_3 nanorods were then annealed in air for 3 h at 400 °C to stabilize the crystalline structures. Photograph of the fabricated sensor is displayed in the inset of Fig. 1.

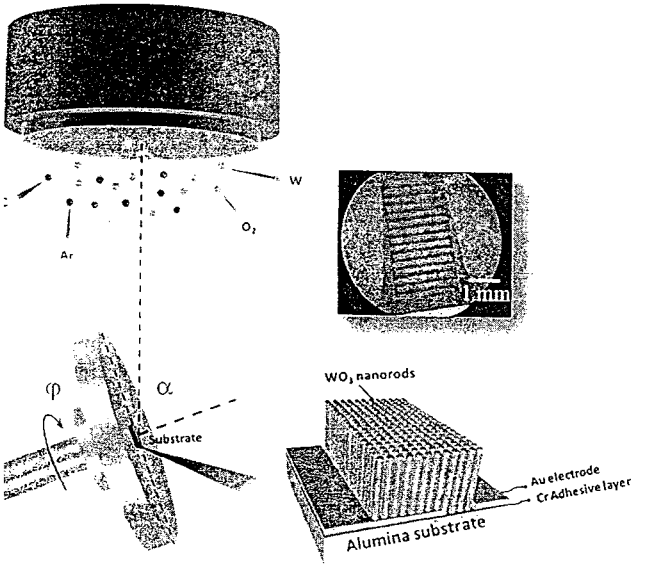

Fig. 1. Schematic of the carbon-doped WO_3 nanorods array fabricated by the glancing-angle RF magnetron sputtering deposition. Inset shows photograph of Au electrode with sensing layer.

2.2. Characterization

The morphology, chemical composition and crystallographic structure of carbon-doped and undoped WO_3 nanorods were characterized using a field emission scanning electron microscopy (FE-SEM, Hitachi S-4700), Auger electron spectroscopy (AES, EMSL 680), and X-ray diffraction (XRD, Rigaku Ttrax III). SEM and AES characterizations were conducted at an electron acceleration voltage of 10 kV. Prior to AES measurement, the surface of WO_3 nanorods was sputtered to clean surface contamination by a 2 keV Argon ion beam for 1 min. Grazing-incidence XRD measurement was operated at 50 kV/300 mA with Cu-$K_{\alpha 1}$ radiation ($\lambda = 1.54056$ Å). The detector scanning speed was set at a rate of 1°/min and the measurement was run from 20 to 60° incident angles in steps of 0.02°.

2.3. Gas sensing measurements

The gas sensing properties of the undoped and carbon-doped WO_3 nanorods were measured using a dynamic flow system with gas concentrations controlled by using a mass flow controllers (Brook Instrument Inc.). A set of heaters made of Ni–Cr coils were used to supply a well-controlled operating temperature in the range of 100–300 °C. The sensors were tested by applying a constant voltage (10 V) and measuring electrical current using a 8846 A Fluke multimeter with 6.5 digit resolution. The resistance of gas sensors can be calculated from the simple Ohm's law. The target gases including nitrogen dioxide (NO_2), hydrogen sulfide (H_2S), hydrogen (H_2), ammonia (NH_3), carbon monoxide (CO), and ethanol (EtOH) vapor were introduced at various concentrations to assess the response and selectivity of the sensors. To avoid the humidity effects, the zero-grade dry air was used as the carrier gas. The times for response and recovery period were selected from the times to achieve at least 90% resistance change of the saturated value. The data were recorded every second using LabVIEW via a USB DAQ device for subsequent analyses.

3. Results and discussion

3.1. Characterization of structure and morphology

The surface morphologies of the as-grown products are displayed in Fig. 2. It can be seen that the glancing-angle RF magnetron sputtering deposition technique produces well-aligned WO_3 vertical nanorods with highly uniform distribution over a large area (Fig. 2a). The nanorod structures results in a rougher surface and larger specific surface area compared to undoped ones. The average diameter (Fig. 2b) and length of carbon-doped WO_3 nanorods are

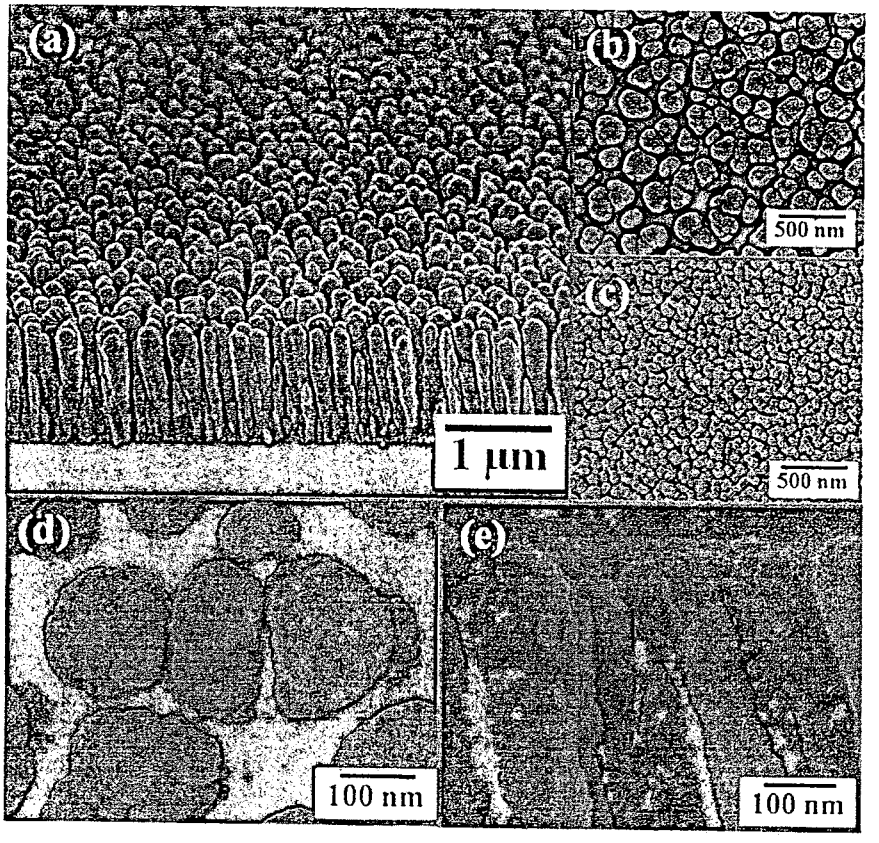

2. FESEM images of (a) side view and (b) top view of carbon-doped WO_3 nanorods, (c) top view of undoped WO_3, (d) and (e) partial wall-wall connections of nanorods.

mated to be ~174 nm and ~1.1 μm, respectively, corresponding n aspect ratio of ~6.3 while the undoped WO_3 nanorods have an rage diameter of ~74 nm (Fig. 2c) and length of ~235 nm, lead- to an aspect ratio of ~3.2. It should be recalled that the time leposition for both structures were three hours. Thus, acety- gas plays an important role in accelerating the growth of WO_3 orods, resulting in nanorod structure with higher aspect ratio. phenomenon may be attributed to the enhancement of local ıbustive oxidation and temperature gradients and more details he carbon-assisted growth mechanism can be found in Ref. . From top-view SEM images at medium and low magnifica- s (Fig. 2b and c), nanorods seem to be isolated and connected ther only at their base. However, more detailed examination lustrated in Fig. 2d and e reveals that nanorods are partially ıected along parts of their walls and the connection occurs inually throughout the nanorod array.

he growth mechanism of nanorods can be schematically illus- ed in Fig. 3. The vertically well-aligned WO_3 nanorods are ıed due to the dominant of strong atomic self-shadowing under litions of limited adatom mobility [38–40]. The growth process be divided into two stages including (I) initial nucleation to ı shadowing centers and (II) formation of columnar structures to the shadowing effect. Initially, deposited atoms are ran- ly distributed on a substrate forming initial nucleation sites. initial nucleated islands behave as the shadowing centers hide unoccupied sites and smaller islands from the incident ır flux arriving at a glancing angle ($\alpha = 85^\circ$). Thus, atoms from ır flux only accumulate on taller islands, which are grown into mns. For materials with the limited adatom mobility such as , voids are not filled due to very slow surface diffusion [38]. efore, the layer consisting of nanorods is formed with sep- on of narrow pores. It should be noted that vapor flux can be divided into vertical and lateral components with respect to substrate. However, the average lateral component becomes zero because of the cancelation of lateral component at opposite direc- tions under a constant-speed substrate rotation, leading to vertical growth [39].

Auger electron spectra of carbon-doped and undoped WO_3 nanorods are demonstrated in Fig. 4. The spectra contain only three existing elements including carbon, tungsten and oxygen.

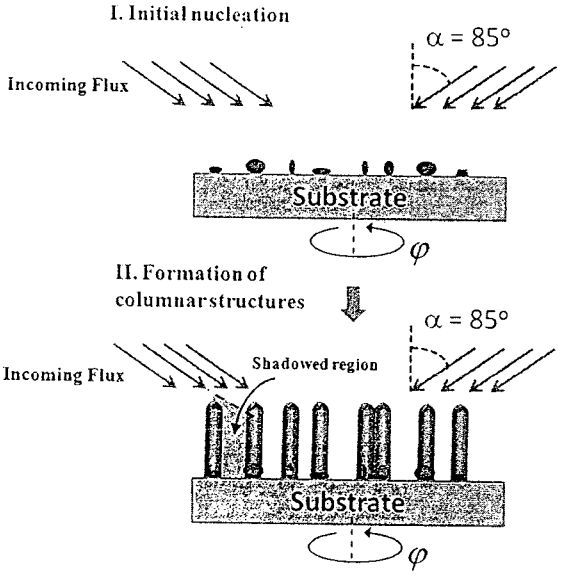

Fig. 3. Model of nanorods formation using GLAD technique.

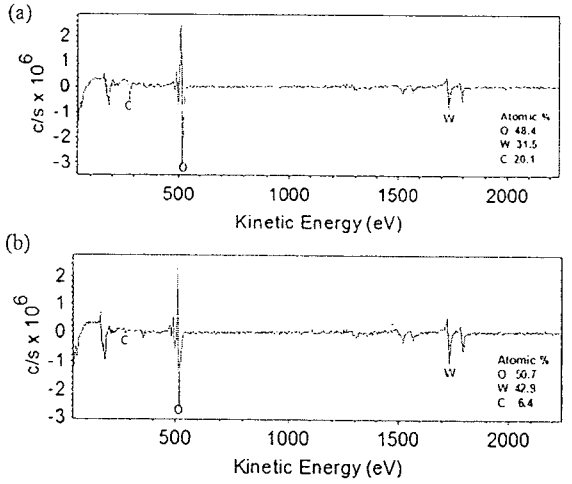

g. 4. Auger electron spectra of (a) carbon-doped and (b) undoped WO_3 nanorods.

he spectrum of carbon doped sample shows apparently higher arbon peak than that of the undoped one and the carbon contents f carbon-doped and undopped are estimated to be 20.1 and 6.4 at% espectively. Thus, the result confirms that carbon is incorporated into WO_3 nanorods and the produced nanorods have high urity without contamination from other elements. Fig. 5 shows RD patterns of carbon-doped and undoped WO_3 nanorods. Both arbon-doped and undoped WO_3 nanorods can be well indexed o the standard pattern of monoclinic WO_3 with lattice constants f $a = 7.297$ Å, $b = 7.539$ Å, and $c = 7.688$ Å (JCPDS No. 43-1035). No eak of impurities is found in these XRD patterns. By using Scherer equation, the average grain size based on the peak from 21.5° to 5.5° can be calculated to be 23 nm and 26 nm for the undoped WO_3 anorods and the carbon-doped WO_3, respectively. Therefore, carbon doping causes a small increase of grain size but does not change he crystallinity of the WO_3 nanorods, which is in agreement with nother report of C doping in WO_3 films [41].

2. Gas sensing properties

The gas-sensing properties of the sensors are primarily characterized in terms of gas response. The gas response to reducing gases .e. H_2, NH_3, CO, H_2S, EtOH) and to oxidizing gases (i.e. NO_2) are efined as R_a/R_{rg} and R_{og}/R_a, respectively, where R_a is the resistance f sensor in pure air, R_{rg} is the resistance of sensor in reducing gas,

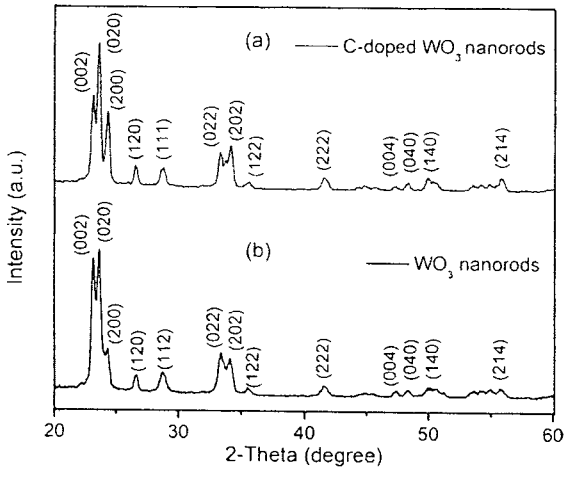

Fig. 5. XRD patterns of (a) carbon-doped and (b) undoped WO_3 nanorods.

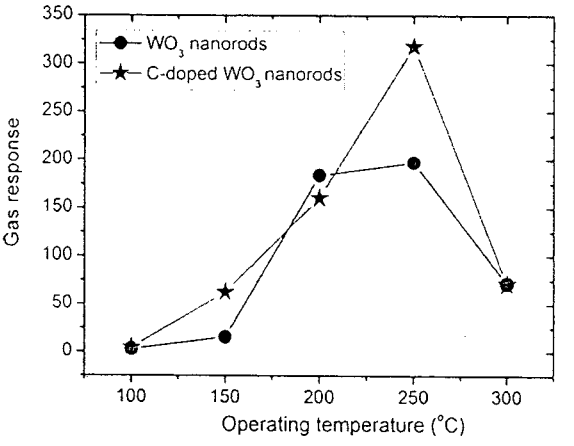

Fig. 6. Operating temperature dependence of gas responses to 3 ppm NO_2.

and R_{og} is the resistance of sensor in oxidizing gas. Fig. 6 shows the gas response of the C-doped and undoped WO_3 nanorods gas sensors to 3 ppm NO_2 at different operating temperatures. It can be seen that the gas responses of both gas sensors increase with increasing operating temperatures from 100 °C to 250 °C and then decrease as the operating temperature increases further. Thus, the optimum operating temperature of both nanorods gas sensors are around 250 °C. In general, the increase of operating temperature contributes to the increase of the adsorption, diffusion and surface reaction rates [22,42]. In other words, sufficient thermal energy helps the reactions involved overcome their respective activation energy barriers leading to increase sensor response with increasing operating temperatures from 100 °C to 250 °C. However, desorption process will dominate and the diffusion depth becomes lower when operating temperature becomes too high leading to the decrease of gas response [43]. This behavior can also be well explained by the diffusion theory [44].

Dynamic response of the carbon-doped and undoped WO_3 nanorods gas sensors toward NO_2 at the optimum operating temperature of 250 °C is illustrated in Fig. 7. It can be seen that both carbon-doped and undoped WO_3 nanorods behave as *n*-type semiconductors since the sensor's resistances increase upon the introduction of oxidizing NO_2 gas. In addition, the resistance of carbon-doped WO_3 nanorods is more than an order of magnitude lower than that of undoped one, indicating a significant increase

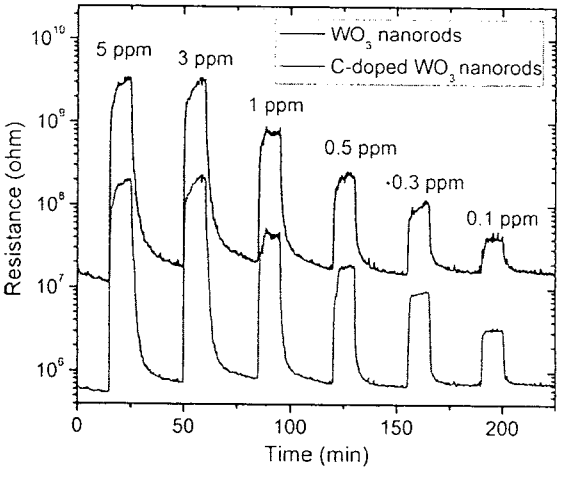

Fig. 7. Dynamic resistance response of the carbon-doped and undoped WO_3 nanorods gas sensors toward NO_2 based on optimum operating temperature of 250 °C.

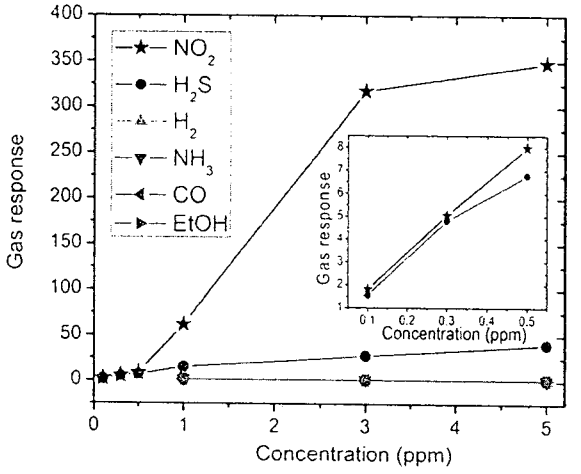

3. Gas responses of carbon-doped WO_3 nanorod gas sensor versus concentra- of different gases. The inset shows the gas responses at low concentrations of and H_2S ranging from 0.1 ppm to 0.5 ppm.

charge carrier concentration due to carbon incorporation. eover, the sensors exhibit fast and stable response toward NO_2. response and recovery times are increased with increasing concentrations. The response times of the carbon-doped and oped WO_3 nanorods gas sensors to 0.1 ppm NO_2 are estimated e 17 s and 21 s, respectively while the corresponding recov- times are 50 s and 69 s. The improved response rate by carbon ing may be attributed to increased adsorption and desorption s of NO_2 molecules on the WO_3 surface due to the increase of ge carriers.

n order to investigate the response and selectivity of C-doped 3 nanorods gas sensor, the sensor was exposed to NO_2, H_2S, H_2, , CO, and EtOH at various concentrations. Various gas responses arbon-doped WO_3 nanorod sensor at the optimum operating perature of 250 °C are displayed in Fig. 8. It can be seen that on-doped WO_3 nanorod sensor exhibits high response to NO_2 s almost insensitive to H_2, NH_3, CO, and EtOH at concentrations ging from 1 ppm to 5 ppm. At the concentration of 5 ppm, the esponse of carbon-doped WO_3 nanorod sensor to NO_2 and H_2S ~348 and ~40. Thus, the sensor clearly shows the selectivity to at concentrations ranging from 1 ppm to 5 ppm. However, the esponse of sensor to NO_2 and H_2S are not significant different ie low concentration range (0.1 and 0.3 ppm, inset of Fig. 8). The ction limit of NO_2 for carbon-doped WO_3 nanorods sensor is nated to be <0.5 ppm at the operating temperature of 250 C. rom Fig. 6, it can also be noticed that carbon-doped WO_3 orods gas sensor exhibits relatively high NO_2 response as com- d to the undoped one at low operating temperature of 150 C. It us useful to evaluate its response at low operating temperature °C) for low-power gas-sensing applications. Fig. 9 shows gas onses of carbon-doped and undoped WO_3 nanorods gas sen- to NO_2 at various gas concentration. It is evident that the gas onses of carbon-doped WO_3 nanorods sensor are considerably er than those of the undoped sensor at all NO_2 concentrations. oncentration of 5 ppm, the gas response of carbon-doped WO_3 orods sensor is ~114, which is ~2 times higher than that of oped WO_3 nanorods sensor (~52). The enhancement of gas onse at low operating temperature after carbon doping may xplained as follows. It was found that carbon doping results ie decrease of sensors resistance at 150 °C from 128 MΩ to MΩ. This may imply the decrease of activation energy barrier charge carrier generation. At low operating temperature, the oped sensor exhibits low conductivity and low gas response use thermal energy is not enough to-overcome the activation

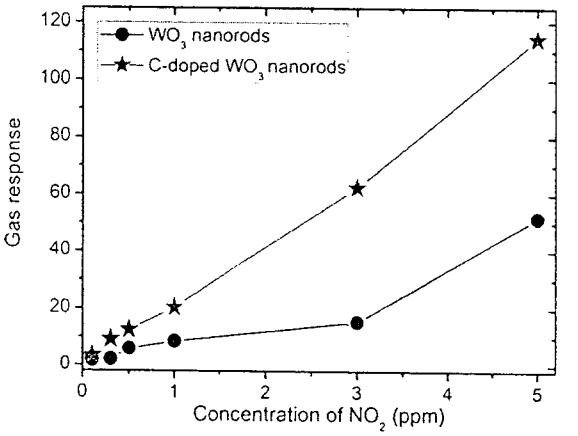

Fig. 9. Gas responses of carbon-doped and undoped WO_3 nanorods gas sensors to different concentrations of NO_2 at the operating temperature of 150 °C.

energy barrier. After carbon doping, the activation energy is reduced and charge carrier can be better thermally activated leading to higher gas response. In addition, the WO_3 nanorods sensor prepared by this method can detect NO_2 at relatively low operating temperature with high gas response compared to some other methods. For example, gas response to 1 ppm NO_2 of our carbon-doped WO_3 nanorods sensor is 18.2 at operating temperature of 150 °C while gas responses of WO_3 nanorods sensors prepared by thermal evaporation [25] and hydrothermal process [45] at their optimum operating temperature of 300 °C were reported to be 7 and 5.3, respectively.

3.3. Sensing mechanism

Based on the observation of FE-SEM (see Fig. 2d and e), nanorods connect together not only at their base but also along some parts of their sidewall. This allows current to flow from one electrode to another electrode with contribution of partial wall-wall nanorods connections as schematically illustrated in a simplified model (Fig. 10a). Thus, the sidewalls of WO_3 nanorods can also contribute to gas-sensing, leading to a large active gas-sensing area and high gas response. This is in agreement with the observed high NO_2 response (300–400), which should not be possible if only base of nanorods takes part in gas-sensing.

From the results, doping of carbon into WO_3 nanorods does not change the crystallinity but it tends to decrease activation energy and alter the thickness of the depletion layer. Sensing mechanism of carbon-doped WO_3 nanorods sensor may therefore be explained based on the model of general WO_3 nanorod sensor [43,46]. The sensing mechanism of NO_2 reactions on the surface of a single C-doped WO_3 nanorod is displayed in Fig. 10b. Initially, oxygen molecules from air adsorb on the surface of C-doped WO_3 nanorods and transform to chemisorbed oxygen species (O^{2-}, O_2^-, and O^-) by trapping the electrons at the surface according to the following reactions [47]:

$$O_2(g) \rightarrow O_2(ads) \quad (1)$$

$$O_2(ads) + e^- \rightarrow O_2^-(ads) \quad (2)$$

$$O_2^-(ads) + e^- \rightarrow 2O^-(ads) \quad (3)$$

$$O^-(ads) + e^- \rightarrow O^{2-}(ads) \quad (4)$$

At the operating temperature of 100–300 °C, the chemisorbed oxygen specie, O^-, is known to be dominant. When O^- species adsorb on surface, a depletion layer known as the space charge layer is formed at grain boundaries near the carbon-doped WO_3 nanorod surface. When a carbon-doped WO_3 nanorod is exposed to NO_2,

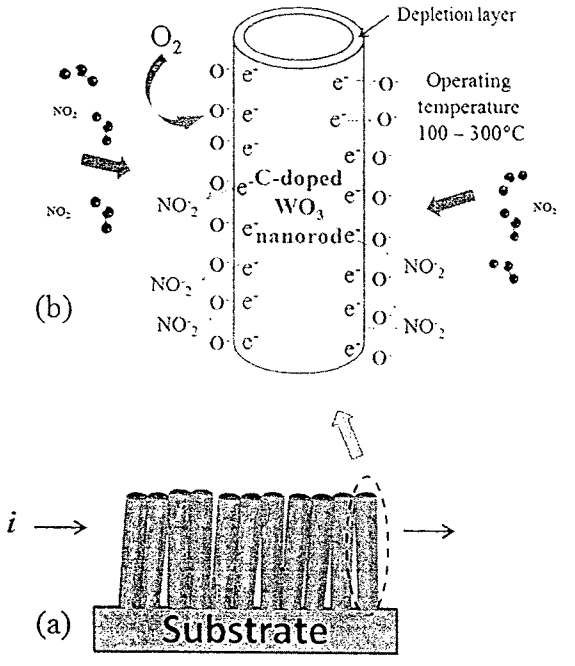

ig. 10. (a) Simplified model of a current flow through WO_3 nanorods from left side o right side and (b) Model of NO_2 reaction on the C-doped WO_3 nanorod surface.

NO_2 molecules directly adsorb on the surface of nanorods because NO_x molecules own very high electron affinity (2.28 eV) compared vith oxygen's value of 0.43 eV [48,49]. Moreover, the products from he reaction between NO_2 and e^- on the surface also react with the O^- species, resulting in the continuously decreasing concentration of electrons on the surface. The process can be described by the ollowing reactions [50]:

$$NO_2(g) + e^- \rightarrow NO_2^-(ads) \quad (5)$$

$$NO_2^-(ads) + 2O^-(ads) \rightarrow 2O^{2-}(ads) + NO_2(g) \quad (6)$$

The above reactions decrease the electrons from carbon-loped WO_3 nanorods and increase the thickness of the depletion ayer, leading to the increase in resistance of carbon-doped WO_3 ıanorods sensor.

4. Conclusion

Carbon-doped and undoped WO_3 nanorods gas sensors have uccessfully been fabricated by the GLAD technique with RF mag-ıetron sputtering. By this technique, the vertically well-aligned ıomogeneous WO_3 nanorods with very low defect were achieved ıver a large area. It was found that carbon doping does not change ıny crystalline structure but increases the grain size and acceler-ıtes the nanorods growth leading to relatively high aspect ratios as ompared to the undoped one. The fabricated carbon-doped WO_3 ıanorods sensor exhibits high response and selectivity to NO_2 at he concentration range of 0.5–5 ppm at an optimum operating emperature of 250 °C. In addition, the carbon-doped sensor still vorks well for NO_2 detection at lower operating temperature of 50 °C due to the decrease of activation energy and alteration of he depletion layer. Therefore, carbon-doped well-ordered WO_3 ıanorods with improved NO_2 gas-sensing performances in terms of response, response time, selectivity and operating temperature ıas been realized. Moreover, our technique offers distinct advan-ages over other methods such as high productivity, simplicity and ow cost for well-ordered nanostructure construction.

Acknowledgments

C.W. acknowledges TRF-CHE-KU Research Grant for New Scholar (MRG 5580229). This work was supported by National Science and Technology Agency, Thailand Research Fund, Kasetsart University and Mahidol University.

References

[1] M. Penza, M.A. Tagliente, L. Mirenghi, C. Gerardi, C. Martucci, G. Cassano, Tungsten trioxide (WO_3) sputtered thin films for a NO_x gas sensor, Sensors and Actuators B 50 (1998) 9–18.
[2] X. Wang, N. Miura, N. Yamazoe, Study of WO_3-based sensing materials for NH_3 and NO detection, Sensors and Actuators B 66 (2000) 74–76.
[3] T.S. Kim, T.B. Kim, K.S. Yoo, G.S. Sung, H.J. Jung, Sensing characteristics of dc reactive sputtered WO_3 thin films as an NO_x gas sensor, Sensors and Actuators B 62 (2000) 102–108.
[4] K.M. Sawicka, A.K. Prasad, P.I. Gouma, Metal oxide nanowires for use in chemical sensing applications, Sensor Letters 3 (2005) 31–35.
[5] W.H. Tao, C.H. Tsai, H_2S sensing properties of noble metal doped WO_3 thin film sensor fabricated by micromachining, Sensors and Actuators B 81 (2002) 237–247.
[6] B. Frühberger, M. Grunze, D.J. Dwyer, Surface chemistry of H_2S-sensitive tungsten oxide films, Sensors and Actuators B 31 (1996) 167–174.
[7] A. Hoel, L.F. Reyes, P. Heszler, V. Lantto, C.G. Granqvist, Nanomaterials for environmental applications: novel WO_3-based gas sensors made by advanced gas deposition, Current Applied Physics 4 (2004) 547–553.
[8] R. Ionescu, A. Hoel, C.G. Granqvist, E. Llobet, P. Heszler, Low-level detection of ethanol and H_2S with temperature-modulated WO_3 nanoparticle gas sensors, Sensors and Actuators B 104 (2005) 132–139.
[9] X. Li, G. Zhang, F. Cheng, B. Guo, J. Chen, Synthesis, characterization, and gas-sensor application of WO_3 nanocuboids, Journal of the Electrochemical Society 153 (2006) 133–137.
[10] Y. Xu, Z. Tang, Z. Zhang, Y. Ji, Z. Zhou, Large-scale hydrothermal synthesis of tungsten trioxide nanowires and their gas sensing properties, Sensor Letters 6 (2008) 938–941.
[11] G. Neri, G. Micali, A. Bonavita, S. Ipsale, G. Rizzo, M. Niederberger, N. Pinna, Tungsten oxide nanowires-based ammonia gas sensors, Sensor Letters 6 (2008) 590–595.
[12] E. Llobet, G. Molas, P. Molinàs, J. Calderer, X. Vilanova, J. Brezmes, J.E. Sueiras, X. Correig, Fabrication of highly selective tungsten oxide ammonia sensors, Journal of the Electrochemical Society 147 (2000) 776–779.
[13] C. Balázsia, L. Wang, E.O. Zayim, I.M. Szilágyid, K. Sedlackovác, J. Pfeifera, A.L. Tótha, P.I. Goumab, Nanosize hexagonal tungsten oxide for gas sensing applications, Journal of the European Ceramic Society 28 (2008) 913–917.
[14] U. Wang, J. Pfeifer, C. Balazsi, P.I. Gouma, Synthesis and sensing properties to NH_3 of hexagonal WO_3 metastable nanopowders, Materials and Manufacturing Processes 22 (2007) 773–776.
[15] O. Berger, T. Hoffmann, W.-J. Fischer, V. Melev, Tungsten-oxide thin films as novel materials with high sensitivity and selectivity to NO_2, O_3, and H_2S. Part II: application as gas sensors, Journal of Materials Science: Materials in Electronics 15 (2004) 483–493.
[16] V. Aroutiounian, Metal oxide hydrogen, oxygen, and carbon monoxide sensors for hydrogen setups and cells, International Journal of Hydrogen Energy 32 (2007) 1145–1158.
[17] A. Ahmad, J. Walsh, Development of WO_3-based thick-film hydrogen sensors, ECS Transactions 3 (2006) 141–152.
[18] S.J. Ippolito, S. Kandasamy, K. Kalantar-zadeh, W. Wlodarski, Hydrogen sensing characteristics of WO_3 thin film conductometric sensors activated by Pt and Au catalysts, Sensors and Actuators B 108 (2005) 154–158.
[19] W.C. Hsu, C.C. Chan, C.H. Peng, C.C. Chang, Hydrogen sensing characteristics of an electrodeposited WO_3 thin film gasochromic sensor activated by Pt catalyst, Thin Solid Films 516 (2007) 407–411.
[20] S. Fardindoost, A. Iraji-zad, F. Rahimi, R. Ghasempour, Pd doped WO_3 films prepared by sol-gel process for hydrogen sensing, International Journal of Hydrogen Energy 35 (2010) 854–860.
[21] H. Nakagawa, N. Yamamoto, S. Okazaki, T. Chinzei, S. Asakura, A room-temperature operated hydrogen leak sensor, Sensors and Actuators B 93 (2003) 468–474.
[22] C. Wongchoosuk, A. Wisitsoraat, D. Phokharatkul, A. Tuantranont, T. Kerdcharoen, Multi-walled carbon nanotube-doped tungsten oxide thin films for hydrogen gas sensing, Sensors 10 (2010) 7705–7715.
[23] X. Ding, D. Zeng, S. Zhang, C. Xie, C-doped WO_3 microtubes assembled by nanoparticles with ultrahigh sensitivity to toluene at low operating temperature, Sensors and Actuators B 155 (2011) 86–92.
[24] T. Siciliano, A. Tepore, G. Micocci, A. Serra, D. Manno, E. Filippo, WO_3 gas sensors prepared by thermal oxidization of tungsten, Sensors and Actuators B 133 (2008) 321–326.
[25] S. An, S. Park, H. Ko, C. Lee, Enhanced NO_2 gas sensing properties of WO_3 nanorods encapsulated with ZnO, Applied Physics A: Materials Science and Processing 108 (2012) 53–58.

[B. Cao, J. Chen, X. Tang, W. Zhou, Growth of monoclinic WO_3 nanowire array for highly sensitive NO_2 detection, Journal of Materials Chemistry 19 (2009) 2323–2327.
[M. Righettoni, A. Tricoli, S.E. Pratsinis, Si:WO_3 Sensors for highly selective detection of acetone for easy diagnosis of diabetes by breath analysis, Analytical Chemistry 82 (2010) 3581–3587.
S. Ashraf, C.S. Blackman, R.G. Palgrave, S.C. Naisbitt, I.P. Parkin, Aerosol assisted chemical vapour deposition of WO_3 thin films from tungsten hexacarbonyl and their gas sensing properties, Journal of Materials Chemistry 17 (2007) 3708–3713.
S. Vallejos, T. Stoycheva, P. Umek, C. Navio, R. Snyders, C. Bittencourt, E. Llobet, C. Blackman, S. Moniz, X. Correig, Au nanoparticle-functionalised WO_3 nanoneedles and their application in high sensitivity gas sensor devices, Chemical Communications 47 (2011) 565–567.
W. Smith, A. Wolcott, R.C. Fitzmorris, J.Z. Zhang, Y. Zhao, Quasi-core–shell TiO_2/WO_3 and WO_3/TiO_2 nanorod arrays fabricated by glancing angle deposition for solar water splitting, Journal of Materials Chemistry 21 (2011) 10792–10800.
W.J. Khudhayer, N. Kariuki, D.J. Myers, A.U. Shaikh, T. Karabacak, GLAD Cr nanorods coated with SAD Pt thin film for oxygen reduction reaction, Journal of the Electrochemical Society 159 (2012) 729–736.
Y. He, Y. Zhao, Mg nanostructures tailored by glancing angle deposition, Crystal Growth and Design 10 (2010) 440–448.
L. González-García, I. González-Valls, M. Lira-Cantu, A. Barranco, A.R. González-Elipe, Aligned TiO_2 nanocolumnar layers prepared by PVD-GLAD for transparent dye sensitized solar cells, Energy and Environmental Science 4 (2011) 3426–3435.
D. Deniz, D.J. Frankel, R.J. Lad, Nanostructured tungsten and tungsten trioxide films prepared by glancing angle deposition, Thin Solid Films 518 (2010) 4095–4099.
D. Deniz, R.J. Lad, Temperature threshold for nanorod structuring of metal and oxide films grown by glancing angle deposition, Journal of Vacuum Science and Technology A 29 (2011) 011020.
R. Figueroa, T.G.S. Cruz, A. Gorenstein, WO_3 pillar-type and helical-type thin film structures to be used in microbatteries, Journal of Power Sources 172 (2007) 422–427.
S.H. Li, X.F. Zhu, Y.P. Zhao, Carbon-assisted growth of SiO_x nanowires, Journal of Physical Chemistry B 108 (2004) 17032–17041.
K. Robbie, M.J. Brett, Sculptured thin films and glancing angle deposition: growth mechanics and applications, Journal of Vacuum Science and Technology A 15 (1997) 1460–1465.
Y.P. Zhao, D.X. Ye, G.C. Wang, T.M. Lu, Designing nanostructures by glancing angle deposition, Proceedings of SPIE 5219 (2003) 59–73.
C.M. Zhou, D. Gall, Development of two-level porosity during glancing angle deposition, Journal of Applied Physics 103 (2008) 014307.
Y. Sun, R. Rajpura, D. Raftery, Photoelectrochemical and structural characterization of carbon-doped In_2O_3 and carbon-doped WO_3 films prepared via spray pyrolysis, Proceedings of SPIE 7408 (2009) 74080D.
L. You, Y.F. Sun, J. Ma, Y. Guan, J.M. Sun, Y. Du, G.Y. Lu, Highly sensitive NO_2 sensor based on square-like tungsten oxide prepared with hydrothermal treatment, Sensors and Actuators B 157 (2011) 401–407.
S. Bai, K. Zhang, R. Luo, D. Li, A. Chena, C.C. Liu, Low-temperature hydrothermal synthesis of WO_3 nanorods and their sensing properties for NO_2, Journal of Materials Chemistry 22 (2012) 12643–12650.
G. Sakai, N. Matsunaga, K. Shimanoe, N. Yamazoe, Theory of gas-diffusion controlled sensitivity for thin film semiconductor gas sensor, Sensors and Actuators B 80 (2001) 125–131.
X. An, J.C. Yu, Y. Wang, Y. Hu, X. Yu, G. Zhang, WO_3 nanorods/graphene nanocomposites for high-efficiency visible-light-driven photocatalysis and NO_2 gas sensing, Journal of Materials Chemistry 22 (2012) 8525–8531.
Q. Xiang, G.F. Meng, H.B. Zhao, Y. Zhang, H. Li, W.J. Ma, J.Q. Xu, Au nanoparticle modified WO_3 nanorods with their enhanced properties for photocatalysis and gas sensing, Journal of Physical Chemistry C 114 (2010) 2049–2055.
K. Wetchakun, T. Samerjai, N. Tamaekong, C. Liewhiran, C. Siriwong, V. Kruefu, A. Wisitsoraat, A. Tuantranont, S. Phanichphant, Semiconducting metal oxides as sensors for environmentally hazardous gases, Sensors and Actuators B 160 (2011) 580–591.
[48] P. Broqvist, H. Gronbeck, E. Fridell, I. Panas, NO_x storage on BaO: theory and experiment, Catalysis Today 96 (2004) 71–78.
[49] A. Afzal, N. Cioffi, L. Sabbatini, L. Torsi, NO_x sensors based on semiconducting metal oxide nanostructures: progress and perspectives, Sensors and Actuators B 171/172 (2012) 25–42.
[50] P. Rai, Y.S. Kim, H.M. Song, M.K. Song, Y.T. Yu, The role of gold catalyst on the sensing behavior of ZnO nanorods for CO and NO_2 gases, Sensors and Actuators B 165 (2012) 133–142.

Biographies

Chatchawal Wongchoosuk received the PhD and MSc degrees from Mahidol University and the BSc degree with first class honors in Physics from Prince of Songkla University, Thailand in 2011, 2007, and 2005, respectively. Currently, he is a lecturer at Department of Physics, Faculty of Science, Kasetsart University, Bangkok, Thailand. His research interests cover the topics of modern Nanoscience and Nanotechnology researches ranging from theoretical modeling of nanomaterials to fabrication of intelligent nanodevices such as hybrid gas sensors, electronic nose, printed electronics, 3D-nanostructures.

Anurat Wisitsoraat received his PhD, MS degrees from Vanderbilt University, TN, USA, and BEng degree in electrical engineering from Chulalongkorn University, Bangkok, Thailand in 2002, 1997, and 1993, respectively. His research interests include microelectronic fabrication, semiconductor devices, electronic and optical thin film coating, sensors, and micro electromechanical systems (MEMS).

Ditsayut Phokharatkul is an assistant researcher at MEMS Laboratory in NECTEC, Thailand. He received his BE and ME degrees from Nagoya University (Japan) in 2006 and 2008, respectively. His dissertation is development of high density horizontally aligned carbon nanotubes for CNT-FET application. His research interests include microelectronic fabrication, semiconductor devices, carbon nanotubes, graphene and sensors.

Mati Horprathum received PhD degree in Physics from King Mongkut's University of Technology Thonburi (KMUTT), Thailand in 2009. He did his 1-year postdoctoral study at Laboratory of Atomic Scale Materials Processing, Institute of Scientific and Industrial Research (ISIR), Osaka University, Japan. He is now a research assistant at Optical Thin-Film Laboratory, National Electronic and Computer Technology Center (NECTEC), Thailand. His research interests include glancing-angle deposition, nano-microelectronic mechanic device, surface enhance Raman spectroscopy (SERS), fabrication and characterization of nanostructures, electrochromic thin film, vacuum design and thin film characterization.

Adisorn Tuantranont received the BS degree in electrical engineering from King Mongkut's Institute of Technology Ladkrabang, Thailand, in 1995, and the MS and PhD degrees in electrical engineering from the University of Colorado at Boulder in 2001. Since 2001, he has been the director of the Nanoelectronics and MEMS Laboratory, National Electronic and Computer Technology Center (NECTEC), Pathumthani, Thailand. His research interests are in the area of micro electro-mechanical systems (MEMS), nanoelectronics, lab-on-a-chip technology and printed electronics. He has authored more than 50-refereed journals, 150 proceedings, and holds five patents. He also received the Young Technologist Award in 2004 from the Foundation for the Promotion of Science and Technology under the patronage of H.M. the King, Thailand.

Teerakiat Kerdcharoen received BSc and MSc in Chemistry from Chulalongkorn University in 1990 and 1992, respectively. As an Exchange Student, he received his PhD in Physical Chemistry from University of Innsbruck in 1995. Presently, he is a faculty member of Mahidol University. His research interests cover the topics of organic electronics ranging from theoretical modeling of materials to fabrication of devices such as tactile and chemical sensors.

Lab on a Chip

Electronic Nose for Toxic Gas Detection based on Photostimulated Core-Shell Nanowires

Journal:	*Lab on a Chip*
Manuscript ID:	LC-ART-06-2014-000724
Article Type:	Paper
Date Submitted by the Author:	20-Jun-2014

Complete List of Authors:	Wongchoosuk, Chatchawal; Kasetsart University, Physics; Institute of Microsystems Engineering (IMTEK), Laboratory for Nanotechnology Subannajui, Kittitat; Institute of Microsystems Engineering (IMTEK), Laboratory for Nanotechnology; Mahidol University, Material science and Engineering Program Wang, Chunyu; Fraunhofer-Institute for Applied Solid-State Physics, Yang, Yang; Institute of Microsystems Engineering (IMTEK), Laboratory for Nanotechnology; Nanjing Tech University, State Key Laboratory of Materials-Oriented Chemical Engineering Güder, Firat; Institute of Microsystems Engineering (IMTEK), Laboratory for Nanotechnology Kerdcharoen, Teerakiat; Mahidol University, Physics Cimalla, Volker; Fraunhofer-Institute for Applied Solid-State Physics, Zacharias, Margit; Institute of Microsystems Engineering (IMTEK), Laboratory for Nanotechnology

Electronic Nose for Toxic Gas Detection based on Photostimulated Core-Shell Nanowires

Chatchawal Wongchoosuk[1,2,*], Kittitat Subannajui[2,3], Chunyu Wang[4], Yang Yang[2,5], Firat Güder[2], Teerakiat Kerdcharoen[6], Volker Cimalla[4], Margit Zacharias[2]

[1]Department of Physics, Faculty of Science, Kasetsart University, Bangkok 10900, Thailand

[2]Laboratory for Nanotechnology, Institute of Microsystems Engineering (IMTEK), Albert Ludwigs University, Freiburg 79110, Germany

[3]Material science and Engineering Program, Faculty of Science, Mahidol University, Bangkok 10400, Thailand

[4]Fraunhofer-Institute for Applied Solid-State Physics, Freiburg 79108, Germany

[5]State Key Laboratory of Materials-Oriented Chemical Engineering, College of Chemistry and Chemical Engineering, Nanjing Tech University, Nanjing 210009, China

[6]Department of Physics, Faculty of Science, Mahidol University, Bangkok 10400, Thailand

***Corresponding author**>> E-mail: chatchawal.w@ku.ac.th

Tel.: +662-562-5555; Fax: +662-942-8029

Abstract

A novel fabrication of microelectronic nose based on ZnO nanowires and ZnO surface modifications including ZnO-$ZnAl_2O_4$ core-shell nanowires and ZnO-Zn_2TiO_4 core-shell nanowires gas-sensing elements operated at room temperature is reported. By combining vapor-phase transport processes and atomic layer deposition techniques, highly homogeneous core-shell nanowires structures can be successfully obtained on large scale areas. Under ultraviolet illumination on the specific oxide surfaces, photo-stimulated oxygen species ($O_2^-(ads)$) response and dominate the gas sensing mechanism of the core-shell nanowire at room temperature. Principal component analysis results show the perfect discrimination of gases including toxic gases and non-toxic gases. This novel device can be used to identify both the gas type and the concentration of the gases with concentrations in the ppb level at room temperature.

Keywords: E-nose, Gas Sensor, 1D Nanostructures, ZnO, Kirkendall Effect

1. Introduction

Since more than a decade, so-called electronic noses (E-noses) became a very well-known practical device for sensing technology. With the ability to identify many detecting substances. E-noses are now widely used in several branches of science and engineering, for examples. biosensor E-nose, gas sensor E-nose, or liquid sensor E-nose [1-5]. Although originally it was created in analogy to 'a nose', the application of E-nose is far better than a natural nose in term of quantity analysis. Furthermore E-nose can be used to characterize a substance which might endanger humans.

A normal E-nose is composed of an array of sensors which usually has thin films as sensing receptors. Recently instead of using thin films, E-noses based on nanowires are in the focus of attention. The superior properties in 1D-nanostructure such as a higher surface per volume ratio, potential band-depletion, and surface charge accumulation can provide a better sensitivity with lower power consumption [6]. Therefore, attempts to produce nanowire based E-noses have been increasing. In order to fabricate nanowire sensor arrays, sets of sensors based on different materials are normally combined. An example was shown for instance by Chen et al. [7]. Carbon nanotubes, In_2O_3, SnO_2 and ZnO nanowires were used to act as different selective sensing material on the same E-nose platform. Baik et al. demonstrated a method to obtain an E-nose from a single material, i.e. SnO_2 nanowires, with different metallic decorations on the surface [8]. Despite of the progress accomplished most of nanowire E-nose still requires high operating temperatures (>200 °C). In this paper, we report the development of photo-stimulated E-noses based on pristine ZnO nanowires and surface reconstruction of ZnO nanowires including ZnO-$ZnAl_2O_4$ core-shell and ZnO-Zn_2TiO_4 core-shell nanowires that work at room temperature

for detecting toxic gases. The sensing mechanism of the core-shell nanowires under photo-activation will be discussed in details.

2. Experimental details

The fabrication of the respective ZnO NW based E-nose started with the preparation of a 100 nm dry oxide (SiO_2) as insulated layer on a Si wafer accomplished in the usual way. The Cr (5 nm): Au (100 nm) interdigitated electrode array (IDA) with comb-like pattern was then fabricated on the insulator by conventional photolithography. The produced IDA was cleaned with acetone, isopropanol, and deionized water, and was dried with N_2. In order to establish the sensing materials, ZnO nanowires were directly grown on the IDA by vapor-phase transport process. Note that the ZnO nanowires selectively grow on the lithographically structured Au layer of IDA while the density and thickness of the ZnO nanowires can be well controlled by fixed optimum growth conditions [9]. Briefly, a mixture of ZnO and graphite powders in a 1:1 ratio by weight was placed at the 950 °C position of the horizontal (vacuum tight) two-zone the furnace as vapor source and the IDA at the 750 °C position as substrate. The NW synthesis was carried out at 30 mbar under a constant flow rate of 30 sccm Ar (99.9999%) and 1.5 sccm Ar/O_2 mixture (Ar/O_2 ration of 90/10, purity 99.999%) for 20 min. By vapor phase deposition, the ZnO NWs grew densely and perpendicular or slightly tilted on the electrodes. Hence, at the inter-digitated pads, the ZnO NWs grow across the electrodes with many touching points air-bridged between the nanowires from adjacent contact pads forming a metal-semiconductor-semiconductor-metal device. The sensing of ZnO NWs results from resistance modulation of the ZnO NWs across two electrodes as shown in the schematic device in Fig. 1a. To further establish different sensing materials, the ZnO nanowires were coated homogeneously with 5 nm oxides

such as Al_2O_3 and TiO_2 by atomic layer deposition (ALD) to obtain core-shell nanostructures. The Al_2O_3 and TiO_2 were formed at 115 °C by reacting trimethylaluminum or titanium isopropoxide, respectively, with water vapor in a vertical flow type reactor (OpAL, Oxford Instruments). The coated samples were subsequently annealed at 700 °C for 3 h to achieve $ZnAl_2O_4$ or Zn_2TiO_4 on the surface of ZnO nanowires, respectively, based on solid-state reactions [10].

All three NWs gas sensors including the ZnO, ZnO-$ZnAl_2O_4$ core-shell, and ZnO-Zn_2TiO_4 core-shell NWs sensing parts were used to characterize toxic and non-toxic gases at room temperature. A UV LED ($\lambda \sim 356$ nm and optical power ~ 200 μW) was mounted above the sensors for photo-stimulation. These gas sensor array will be later integrated on the handling PCB for an E-nose. Before introducing gases into the measuring chamber, the chamber was evacuated down to ~10^{-3} mbar, followed by purging of sythesized air. This cycle was repeated several times. After that, different gases, such as O_3, CO and NO_2 with a concentration between 100 ppb and 1 ppm and O_2 with a concentration of 5% to 80% in nitrogen were individually led into the chamber adjusted by mass flow controller. During sensing, the UV LED was switched off in present of target gases and was switched on when the target gas was removed. Theoretically, a large photocurrent will be induced by switching on/off the above-band-gap excitation due to photogenerated carriers [11]. The resistance minima in absent of target gas (R_0) and maxima in target gas (R_G) of the nanomaterials were recorded and the response of the sensor (S) is defined as ($S= |(R_G-R_0)/R_0| \times 100\%$). Next, the sensor response data from all sensors were introduced into principal component analysis (PCA) to provide classification/qualification results of the sensors upon toxic and non-toxic gases. The PCA is a multivariate technique that

transforms the overall information into a set of new linear combinations of orthogonal variables called principal components (PC) without heavy loss of important original information.

3. Results and Discussion

The electrode was designed with a gap size between adjacent electrodes of 3 μm as shown in the inset of Fig. 1b. After the growth of ZnO NWs, adjacent electrodes are electrically connected by cross ZnO NWs (Fig. 1c). The diameter and length of ZnO NWs were in the range of 60-180 nm and a few tens of μm, respectively. As one can see in the inset of Fig. 1c, the ZnO NWs are self-assembled between the gaps of electrodes. This electrical connection by a simple self-assembly process during synthesis reduces tedious and time consuming task comparing with other nanowire-based gas sensor fabrication techniques [12-14]. With the growth condition used here in our vapor phase deposition chamber, the density of ZnO NWs is also well-controlled. The nanowires are single-crystalline with the typical [0002] elongation (*c*-oriented) and follow the VS growth mechanism as shown in Fig. 2a.

To investigate formation of ZnO-$ZnAl_2O_4$ core-shell and ZnO-Zn_2TiO_4 core-shell nanowires, Fig. 2b and 2c presents the TEM images of structures after annealing ZnO-Al_2O_3 and ZnO-TiO_2 nanowires under identical conditions. For ZnO-$ZnAl_2O_4$ core-shell nanowires, cavities distributed along the interface clearly show the existence of bridge-like linkages between the residual ZnO core and the spinel $ZnAl_2O_4$ shell (see Fig. 2b) after solid-solid reaction. The one-way interfacial bulk diffusion of ZnO into the amorphous Al_2O_3 shell can form the $ZnAl_2O_4$ at shell and generate a series of cavities at the interface due to the Kirkendall effect [10]. Unlike the reaction of ZnO-Al_2O_3 nanowires, no cavity was observed at ZnO-Zn_2TiO_4 core-shell interface (see Fig. 2c), indicating the interdiffusion between ZnO and TiO_2 was not dominated by

the Kirkendall effect in this case. Apparently, from the electron diffraction patterns, the unreacted ZnO NWs cores still keep the single-crystal nature while the formed $ZnAl_2O_4$ and Zn_2TiO_4 are polycrystalline with a rough surface feature.

It is well known that the gas sensitivity of ZnO NWs comes from the trapping of the gas molecules on the surface which can modulate the surface depletion layer width [15]. The negative charges at the surface of n-type semiconductor usually generate an upward electronic band-bending along the diameter of ZnO NWs [16]. The surface charges influence the surface-band potential and cause a stronger or a weaker band-bending. This modulation of band-bending directly makes a change in the conduction of ZnO NWs. Figure 3a demonstrates the dynamic responses of nanowires sensors to oxidizing NO_2 gas at room temperature under UV illumination. The electrical resistance of all the sensors increases at the moment of NO_2 exposure. By applying UV illumination during the gas sensing process, electron–hole pairs are generated in sensing materials. The photo-generated holes can migrate to the surface via the electric field induced by the band bending and react with adsorbed oxygen species ($O_2^-(ads)$). At the same time, the photo-generated electrons react with additional photoinduced oxygen ions, resulting to form photostimulated oxygen species ($O_2^-(ads)$) at the shell surfaces as the following schemes [17]:

$$h\nu \rightarrow h^+(h\nu) + e^-(h\nu) \tag{2}$$

$$h^+(h\nu) + O_2^-(ads) \rightarrow O_2(g) \tag{3}$$

$$O_2(g) + e^-(h\nu) \rightarrow O_2^-(h\nu) \tag{4}$$

Upon exposure to NO_2, NO_2 molecules come to react with the photostimulated oxygen species on the surface to capture available free electrons in the following reaction:

$$NO_2(g) + O_2^-(hv) + 2e^-(hv) \rightarrow NO_2^-(ads) + 2O^-(ads) \quad (5)$$

This reaction increases the concentration of holes that enlarged the band bending, leading to an increase of depletion layer width. Therefore, resistance of core-shell nanowire sensor increases with increasing NO_2 concentration. Moreover, NO_2 can also directly capture the electrons from the conduction band due to its higher electrophilic properties [18].

From Fig. 3b, at low NO_2 concentrations (100-300 ppb), the ZnO-Zn_2TiO_4 core-shell nanowire sensor shows high response to NO_2 over other sensors (more than 50%) due to more surface roughness for specific NO_2 adsorptions while it also shows medium sensitivity to O_2 and relatively low sensitivity to CO and O_3. For the ZnO nanowire sensor, it is sensitive to most of gasses. The cross-sensitivity problem makes its selectivity of ZnO nanowire to be low. This may provide an ambiguous response in terms of individual components of the gas mixtures. In case of ZnO-$ZnAl_2O_4$ core-shell nanowires, it exhibits high sensitivity and selectivity to NO_2. This refers to the good performance for NO_2 detection in real world application. The NO_x species prefer to adsorb on the $ZnAl_2O_4$ surface over other gases via π^*(N) transitions [19]. Enhancement of sensing properties of core-shell nanowires over ZnO nanowires may result from the contribution of n–n heterojunction that can adjust energy barrier height and modulate electron transport [20]. In comparison between ZnO-Zn_2TiO_4 and ZnO-$ZnAl_2O_4$ core-shell nanowires, the different sensing properties cause from different rough surface feature and intrinsic material properties. The rough surface feature of the ZnO-Zn_2TiO_4 improves the efficiency and the amount of oxygen chemisorptions [21] resulting in an enhancement of gas responses on all target gases over the ZnO-$ZnAl_2O_4$. The Al_{Zn} antisite defects in $ZnAl_2O_4$ spinel were found to act as a shallow donor and Al-O bond appears more ionic [22]. This can contribute to charge transports between

NO_2 and ZnO-$ZnAl_2O_4$ core-shell nanowires leading to higher selectivity of the ZnO-$ZnAl_2O_4$ core-shell towards NO_2.

To evaluate the discrimination power of core-shell sensor array, the PCA was carried out with the relative response feature extraction technique [2]. As shown in Fig. 4, the PCA result is clearly separated to 4 clusters corresponding to the 4 different target gases. No overlap between different gas species occurs in PCA. It indicates the high performance of such nanowire gas sensor array for detection and discrimination of both oxidizing and reducing gases at room temperature over other pervious work that usually operated at high temperatures (>200 ◦C) [7, 23]. Here we demonstrate that the NW e-nose based on ZnO NWs and surface modification can be used to identify both gas type and the concentration of gases at room temperature. The ZnO NW e-nose which can operate at room temperature will be very useful in term of energy conservation.

4. Conclusion

In summary, we propose a simple but reliable method for the ZnO NW E-nose fabrication. The E-nose composed of three nanowire sensors which are ZnO nanowires, ZnO-ZnO-$ZnAl_2O_4$ core-shell nanowires, and Zn_2TiO_4 core-shell nanowires. The photolithography was used to pattern and identify the ZnO NWs structure. The ZnO NWs were grown by vapor phase deposition and the result from the growth is the cross nanostructure of ZnO NWs between two electrodes. The sensor was then deposited by ALD before annealing process. After an annealing at 700 °C, the solid reactions were completed. All three sensors were used to sense NO_2, CO, O_2, O_3 at room temperature. Based on photostimulation by UV, oxygen species (O_2^-) can be generated to adsopt on the nanowire surface for interacting with gas molecules. The

results shows that ZnO nanowire cannot use as a potential single gas sensor for detection of toxic gas in envelopment at room temperature due to cross sensitive problem of ZnO surface while $ZnAl_2O_4$ surface shows high sensitivity and selectivity to NO_2 and Zn_2TiO_4 exhibits improvement of gas response of toxic gas (NO_2 and CO) at low concentration (100-300 ppb) due to high surface area. By combined three nanowire sensor, the microelectronic nose has great potential to detect and discriminate a wide variety of gases including toxic gases and non-toxic gases.

Acknowledgments

This work was supported by a grant (TRF-CHE-KU Research Grant for New Scholar) from Thailand Research Fund, Commission on Higher Education and Kasetsart University Research and Development Institute (MRG 5580229).

References

[1] G. C. Green, A. D. C. Chan and M. Lin, *Sens. Actuators B,* 2014, **190**, 16-24.

[2] C. Wongchoosuk, A. Wisitsoraat, A. Tuantranont and T. Kerdcharoen, *Sens. Actuators B,* **147**, 392-399.

[3] T. Carvalho, P. Vidinha, B. R.Vieira, R.W. C. Li and J. Gruber, *J. Mater. Chem. C*, 2014, **2**, 696-700.

[4] E. A. Baldwin, J. Bai, A. Plotto and S. Dea, *Sensors*, 2011, **11**, 4744-4766.

[5] W. Ko, N. Jung , M. Lee , M. Yun and S. Jeon, *ACS Nano*, 2013, 7, 6685–6690.

[6] N. S. Ramgir, Y. Yang and M. Zacharias, *Small,* 2010, **6**, 1705–1722.

[7] P. C. Chen, F. N. Ishikawa, H. K. Chang, K. Ryu and C. Zhou, *Nanotechnology*, 2009, **20,** 125503.

[8] J. M. Baik, M. Zielke, M. H. Kim, K. L. Turner, A. M. Wodtke and M. Moskovits, *ACS Nano*, 2010, **4**, 3117-3122.

[9] C. Wongchoosuk, K. Subannajui, A. Menzel, I. Amarilio-Burshtein, S. Tamir, Y. Lifshitz and M. Zacharias, *J. Phys. Chem. C*, 2011, **115**, 757-761.

[10] Y. Yang, D. S. Kim, M. Knez, R. Scholz, A. Berger, E. Pippel, D. Hesse, U. Gösele and M. Zacharias, *J. Phys. Chem.* C, 2008, **112**, 4068–4074.

[11] K. Keem, H. Kim, G. T. Kim, J. S. Lee, B. Min, K. Cho, M. Y. Sung and S. Kim, *Appl. Phys. Lett.*, 2004, **84**, 4376-4378.

[12] J. Chen, K. Wang, R. Huang, T. Saito, Y. H. Ikuhara, T. Hirayama and W. Zhou, *IEEE Trans. Nanotechnol.*, 2010, **9**, 634-639.

[13] S. N. Bai and S. C. Wu, *J. Mater. Sci.: Mater. Electron.*, 2011, **22**, 339–344.

[14] Q. Wan, Q. H. Li, Y. J. Chen, T. H. Wang, X. L. He, J. P. Li and C. L. Lin, *Appl. Phys. Lett.*, 2004, **84**, 3654- 3656.

[15] J. B. K. Law and J. T. L. Thong, *Nanotechnology*, 2008, ***19***, 205502.

[16] S. Chang, I. M. Vitomirov, L. J. Brillson, D. F. Rioux, P. D. Kirchner, G. D. Pettit, J. M. Woodall and M. H. Hecht, *Phys. Rev. B*, 1990, **41**, 12299-12302.

[17] S. W. Fan, A. K. Srivastava and V. P. Dravid, *Appl. Phys. Lett.*, 2009, **95**, 142106.

[18] J. Zhao, T. Yang, Y. Liu, Z. Wang, X. Li, Y. Sun, Y. Du, Y. Li and G. Lu, *Sens. Actuators B*, 2014, **191**, 806–812.

[19] R. Revel, D. Bazin, P. Parent and C. Laffon, *Catal. Lett.*, 2001, **74**, 189- 192.

[20] S. Park, S. An, Y. Mun and C. Lee, *ACS Appl. Mater. Interfaces*, 2013, **5**, 4285–4292.

[21] Y. C. Liang and W. K. Liao, *RSC Adv.*, 2014, **4**, 19482-19487.

[22] H. Dixit, N. Tandon, S. Cottenier, R. Saniz, D. Lamoen and B. Partoens, *Phys. Rev. B*, 2013, **87**, 174101.

[23] V. V. Sysoev, J. Goschnick, T. Schneider, E. Strelcov and A. Kolmakov, *Nano Lett.*, 2007, **7**, 3182-3188.

Lists of Figures

Figure 1: a) Schematic structure of gas sensor for an E-nose. SEM images of b) finger grid interdigitated electrode and c) ZnO NWs grown on the IDA.

Figure 2: TEM images and their corresponding ED patterns of (a) ZnO nanowire, (b) ZnO-$ZnAl_2O_4$ core-shell nanowire, and (c) ZnO-Zn_2TiO_4 core-shell nanowire.

Figure 3: (a) Real time NO_2 detection and (b) responses to various NO_2, CO, O_2, O_3 concentrations of ZnO nanowires, ZnO-$ZnAl_2O_4$ core-shell nanowires, Zn_2TiO_4 core-shell nanowires at room temperature.

Figure 4: 3D principal component analysis plot of three nanowire gas sensors for discriminating a variety of gases at room temperature.

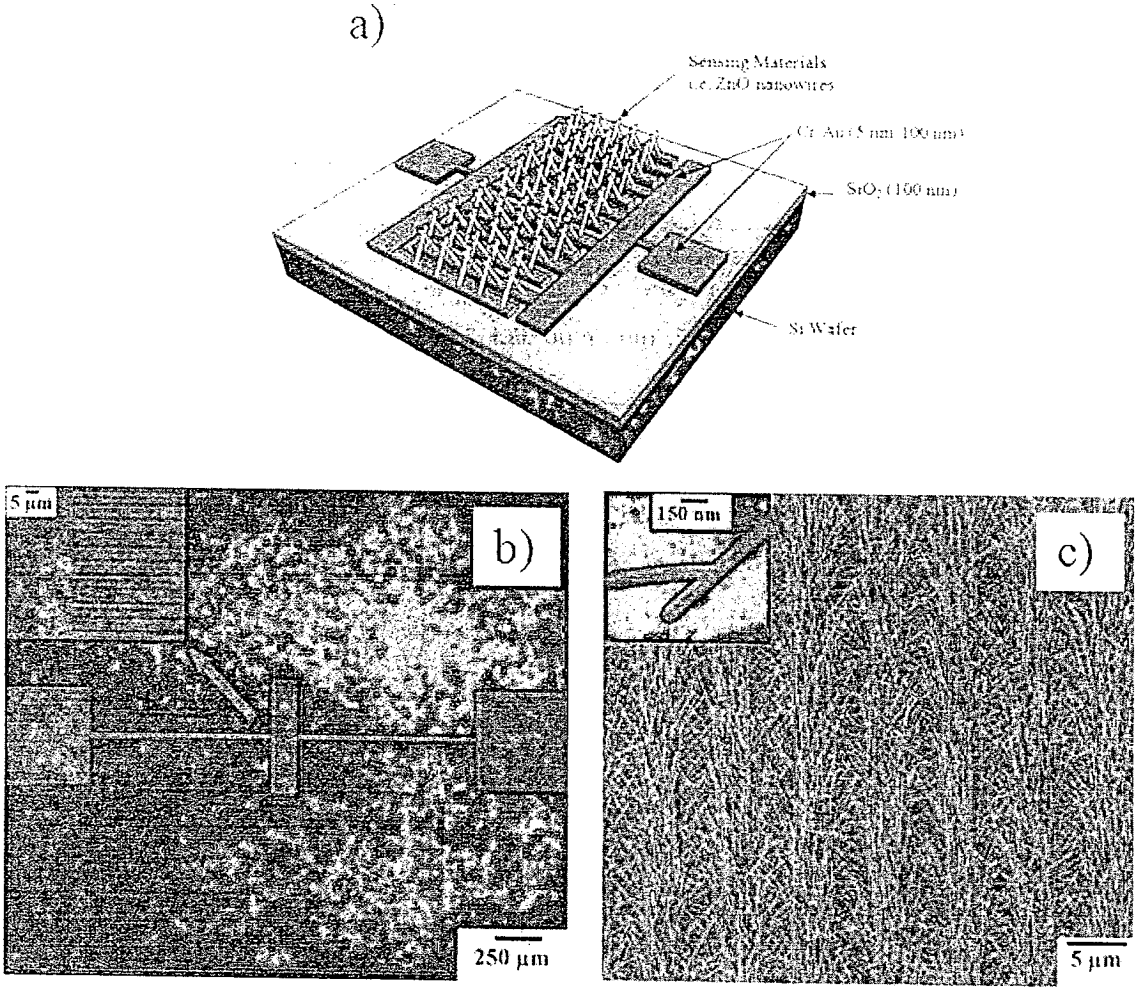
a)
Sensing Materials
(e.g. ZnO nanowires)
Cr/Au (5 nm/100 nm)
SiO_2 (100 nm)
Si Wafer
5 μm
b)
250 μm
150 nm
c)
5 μm

Figure 1

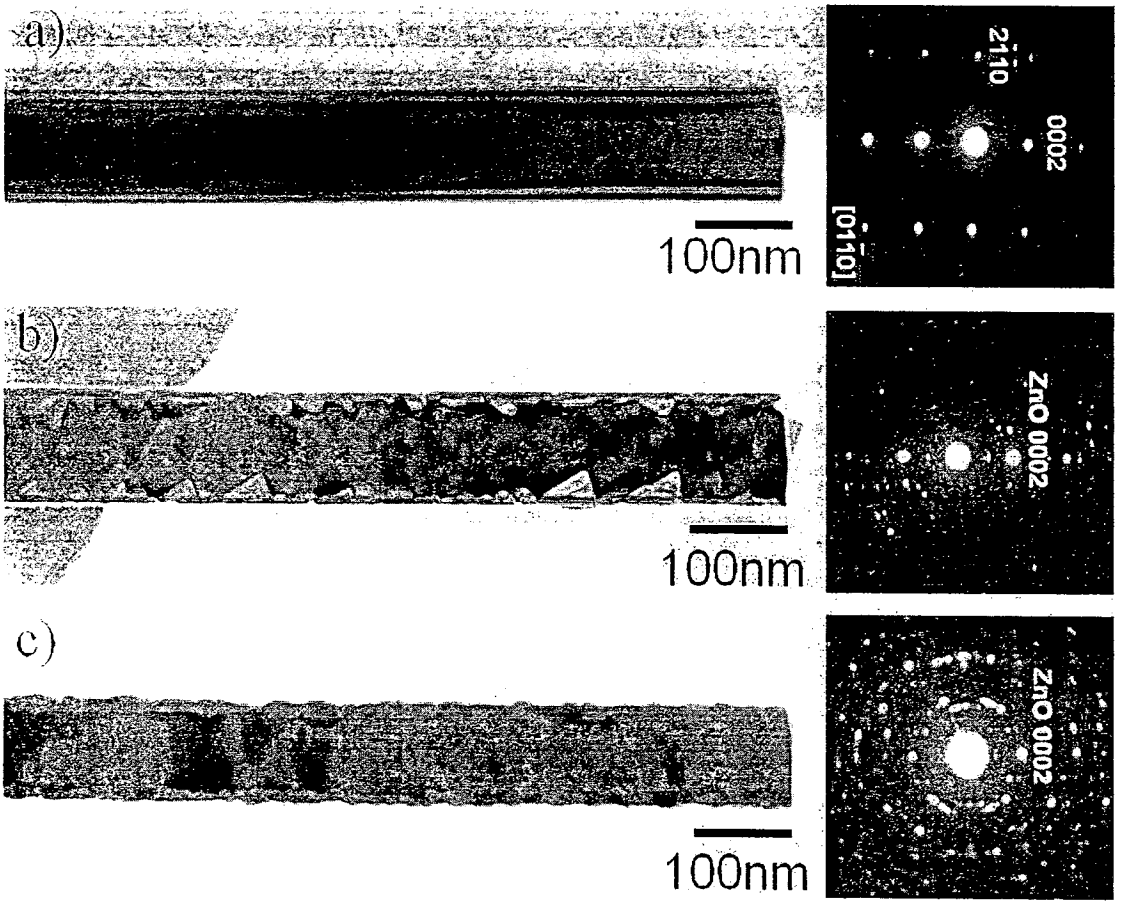
a)
100nm
$2\bar{1}\bar{1}0$
0002
[0110]
b)
100nm
ZnO 0002
c)
100nm
ZnO 0002

Figure 2

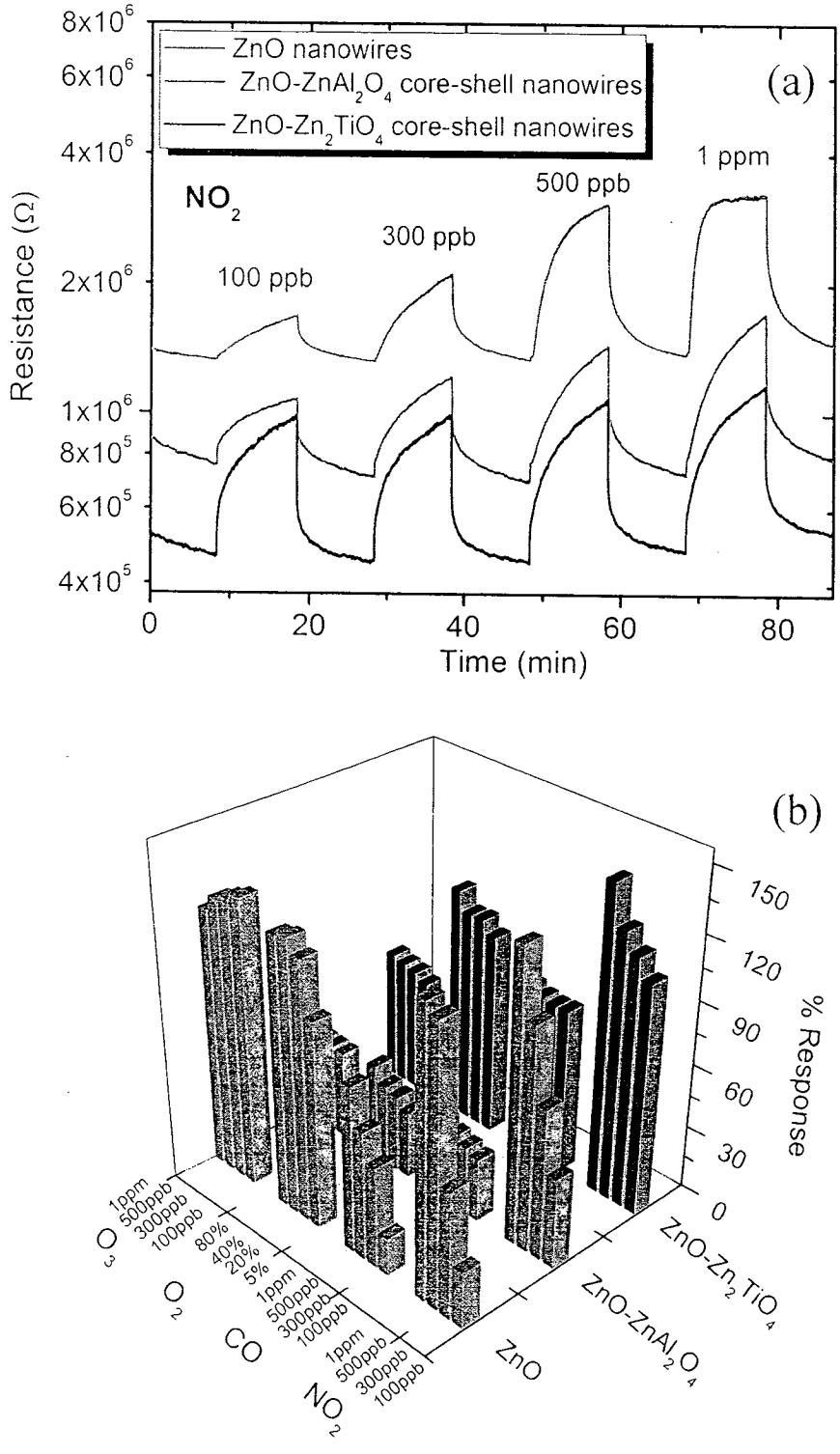
8x10^6
6x10^6
4x10^6
2x10^6
1x10^6
8x10^5
6x10^5
4x10^5
Resistance (Ω)
ZnO nanowires
ZnO-ZnAl2O4 core-shell nanowires
ZnO-Zn2TiO4 core-shell nanowires
(a)
NO2
100 ppb
300 ppb
500 ppb
1 ppm
0
20
40
60
80
Time (min)
(b)
150
120
90
60
30
0
% Response
O3
1ppm
500ppb
300ppb
100ppb
O2
80%
40%
20%
5%
CO
1ppm
500ppb
300ppb
100ppb
NO2
1ppm
500ppb
300ppb
100ppb
ZnO
ZnO-ZnAl2O4
ZnO-Zn2TiO4

Figure 3

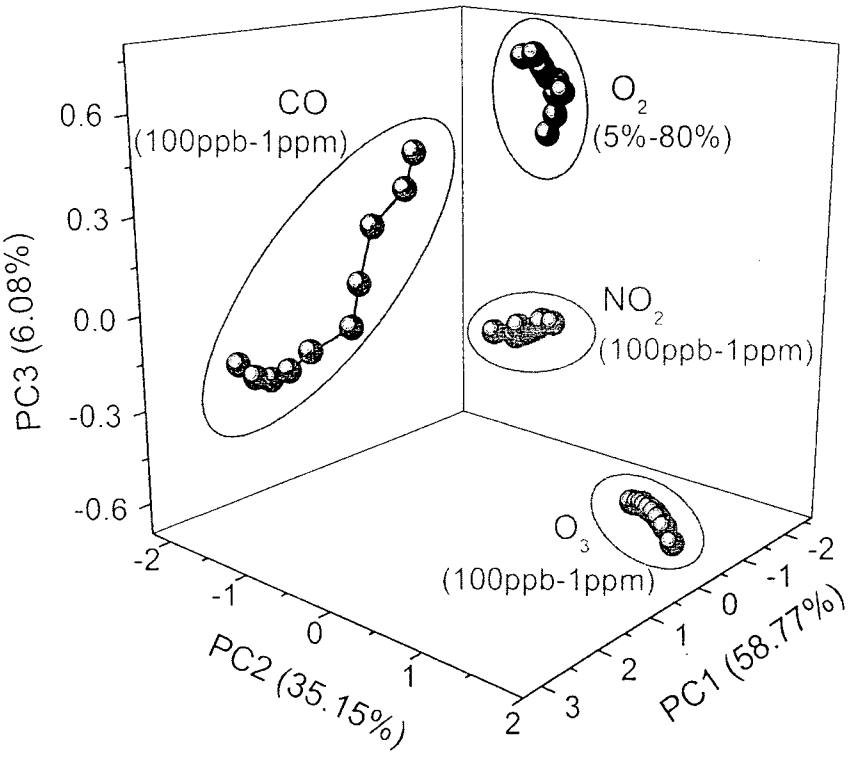
CO
(100ppb-1ppm)
O_2
(5%-80%)
NO_2
(100ppb-1ppm)
O_3
(100ppb-1ppm)
PC3 (6.08%)
0.6
0.3
0.0
-0.3
-0.6
PC2 (35.15%)
-2
-1
0
1
2
PC1 (58.77%)
-2
-1
0
1
2
3

Figure 4

Development of Networked Electronic Nose Based on Multi-walled Carbon Nanotubes/Polymer Composite Gas Sensor Array

Mario Lutz[1], Chatchawal Wongchoosuk[2,*], Adisorn Tuantranont[3], Supab Choopun[4], Pisith Singjai[4], Teerakiat Kerdcharoen[5,6,*]

[1]Materials Science and Engineering Programme, Faculty of Science, Mahidol University, Bangkok, Thailand
[2]Department of Physics, Faculty of Science, Kasetsart University, Bangkok, Thailand, Email: chatchawal@ku.ac.th
[3]Nanoelectronic and MEMS Lab, National Electronic and Computer Technology Center, Pathumthani, Thailand
[4]Department of Physics and Materials Science, Faculty of Science, Chiang Mai University, Chiang Mai, Thailand
[5]Department of Physics and Center of Nanoscience and Nanotechnology, Faculty of Science, Mahidol University, Bangkok, Thailand
[6]NANOTEC Center of Excellence at Mahidol University, National Nanotechnology Center, Email: scitkc@mahidol.ac.th

Abstract

In this paper, we have presented the design and invention of an electronic nose (E-nose) that can work and analyze the results via a network system such as LAN or WiFi. The MWCNTs/polymer composites were used as a gas sensor array. The constant current circuit was newly designed for gas sensor measurement. The fabricated E-nose showed a high performance for indoor air monitoring with very low noise.

Keywords: E-nose, polymer sensor, indoor air monitoring, E-nose circuits, PS/CNT sensor, gas sensor array

Introduction

Recent decades have observed significantly increasing interest in the applications of electronic nose (E-nose) ranging from quality control of foods [1,2] and beverages [3,4], environment protection [5], medical applications [6] to human identification [7,8]. Because E-nose offers many advantages in the analysis of volatiles, i.e. a low detection limit, cost- and time effectiveness, robustness, simplicity, and operator independence [9]. In principles, an E-nose consists of three main parts: (i) air flow system, (ii) detection system, and (iii) control and data analysis system [10]. For air flow system there are two main types of flow systems including static and dynamic flow systems. In detection system, sensor array with measurement circuit is used to detect the aroma molecules. For data analysis system, pattern recognition and machine learning such as artificial neural networks (ANN), linear discriminant analysis (LDA), support vector machine (SVM), and principal components analysis (PCA) are typically used in data analysis on a computer. Although E-nose has been in the market for several years, development of E-nose is still necessary to provide opportunities for new applications.

In this work, we have presented the development of an E-nose that can work and analyze the results via a network system such as LAN and WiFi. The fabrication of room temperature gas sensor array will be proposed. The measurement circuits of the networked E-nose will be highlighted. The constructed networked E-nose will also be demonstrated for uses in real world applications such as indoor air monitoring.

Experimental Details

A. Treatment of Carbon Nanotubes

Multi-walled carbon nanotubes (MWCNTs) were dispersed in a solution of ethanol and NaOH/ethanol using ultrasonication for 30 min. The NaOH/ethanol solution contained 150 g/l of NaOH in 80 vol% ethanol and 20 vol% water. The dispersion was filtered by using a syringe micro-filter system with a nylon micro-filter and then washed with ethanol until the pH value of the filtrate was about 7. After this treatment, the remaining filtered and dried MWNTs can be easily dispersed in different solvents.

B. Preparation of MWCNTs/Polymer Composite Sensor array

The sensor elements consist of interdigitated gold electrodes deposited on aluminum oxide substrate (2x2.5 mm). In order to prepare MWCNTs/polymer composite, polystyrene (PS) and polystyrene-co-maleic acid (PS-Maleic AC) were employed as the polymer matrices while dimethylformamide (DMF) and tetrahydrofuran (THF) were used as solvents. Four different conditions of CNTs/polymer composites were produced as summarized in Table I. The deposition of the CNTs/polymer composites on the sensor element was achieved by drop coating using a micro pipette, Gilson Pipetman P20.

TABLE I
DEPOSITION CONDITIONS FOR THE MWCNTS/POLYMER COMPOSITE COATING

Sensor Number	Polymer / MWCNT	Solvent	Drop amount	Substrate Temp
1	PS	THF	5 µl	80 °C
2	PS	THF	3 µl	80 °C
3	PS-Maleic Ac	THF	3 µl	25 °C
4	PS	DMF	3 µl	80 °C

C. Fabrication of Networked E-nose

The networked E-nose consists of three main parts including

978-1-4673-4842-3/13/$31.00 ©2013 IEEE

(i) air flow system, (ii) detection system, and (iii) control and data analysis system. The air flow system refers to the way to deliver aroma molecules into the detection system. In this networked E-nose, a simple dynamic flow system was employed. The gas sensor array was installed at the bottom of the rectangular chamber. The air carrying the odor molecules can be introduced into the sensor chamber through a hole with an area of 4 cm^2. In the detection system, a constant current circuit as shown in Fig. 1 was used to measure the resistance of the gas sensor array. The constant current measurement circuit consists of an operational amplifier in a constant current configuration of 500 μA with the sensor array to be measured in the feedback loop (see Fig. 1a). Each side of the sensor was connected to a discrete buffer circuit consisting of an operational amplifier in the voltage follower configuration as shown in Fig. 1b. The buffer circuit separates the constant current circuit from the differential amplifier to prevent a disturbance of the current source. The differential amplifier calculates the difference between the two input voltages and multiplies the result by a gain factor. If R3=R4 and R2=R5, the gain factor was R2/R3. In Fig. 1c, R3 and R4 were 1 kΩ while R2 and R5 were 2 kΩ, so the gain factor was 2. For example, if the resistance of the sensor was 1 kΩ, the current of 500 μA produced a voltage difference of 0.5V. Therefore, this voltage difference of 0.5 V was amplified by a factor of 2, so the resulting output voltage was 1V.

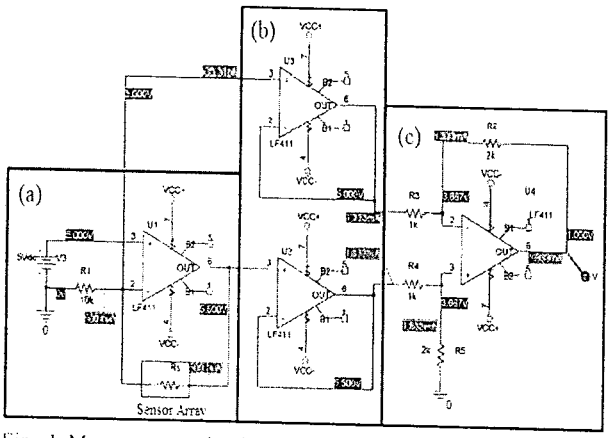

Fig. 1 Measurement circuit with an output of 0-10 V (1 mV/Ω) including (a) 500 μA constant current source, (b) buffer circuit and (c) differential amplifier having gain of 2.

Instead of using a single sensor, an analog multiplexer can be used to select one out of many sensors to be measured as shown in Fig. 2. In such a case, each sensor was connected to one input of the analog 8-channel multiplexer. The multiplexer internally connected only one input to its output. The input-to-output connection was selected by a digital input.

In the control and data analysis system, microchip PIC24FJ 48GA002 microcontroller was used to control the measurement systems. The CS5526 was used as the A/D convertor. The measurement software was written by LabVIEW. The data from networked E-nose was stored and transferred into a Laptop every second via a small WiFi-Router for subsequent analysis.

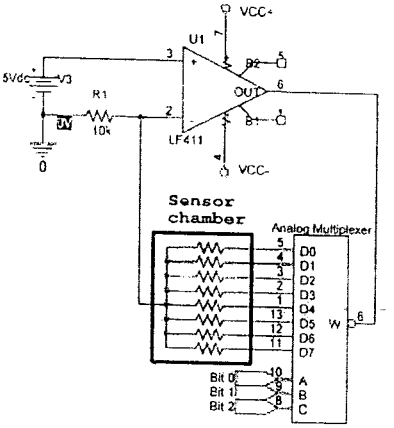

Fig. 2 Connection of gas sensor array with 8-channel multiplexer circuit.

Results and Discussion

A. Electronic Circuit Test

As the design measurement circuits, the sampling rate can be programmed ranging from 3.76 samples per second up to 202 samples per second. Note that the noise level and resolution depends on the sampling frequency.

TABLE II
RMS NOISE OF DESIGN MEASUREMENT CIRCUIT

Output Rate	-3 dB Filter	Input Range (Bipolar/Unipolar Mode)					
(Hz)	Frequency	25 mV	55 mV	100 mV	1 V	2.5 V	5 V
3.76	3.27	90 nV	90 nV	130 nV	1 μV	2 μV	4 μV
7.51	6.55	110 nV	130 nV	190 nV	1.5 μV	3 μV	7 μV
15.0	12.7	170 nV	200 nV	250 nV	2 μV	5 μV	10 μV
30.1	25.4	250 nV	300 nV	500 nV	4 μV	10 μV	15 μV
60.0	50.4	500 nV	1 μV	1.5 μV	15 μV	45 μV	85 μV
123.2	103.6	2 μV	4 μV	8 μV	72 μV	190 μV	350 μV
168.9	141.3	10 μV	20 μV	30 μV	340 μV	900 μV	2 mV
202.3	169.2	30 μV	55 μV	105 μV	1.1 mV	2.4 mV	5.3 mV

TABLE III
RESISTANCE RESOLUTION OF MEASUREMENT CIRCUIT

Output Rate	Resistance Range					
(Hz)	2.5 kΩ	5.5 kΩ	10 kΩ	100 kΩ	250 kΩ	500 kΩ
3.76	0.06 Ω	0.06 Ω	0.09 Ω	0.66 Ω	1.32 Ω	2.64 Ω
7.51	0.07 Ω	0.09 Ω	0.13 Ω	0.99 Ω	1.98 Ω	4.62 Ω
15.0	0.11 Ω	0.13 Ω	0.17 Ω	1.32 Ω	3.3 Ω	6.6 Ω
30.1	0.17 Ω	0.2 Ω	0.33 Ω	2.64 Ω	6.6 Ω	9.9 Ω
60.0	0.33 Ω	0.66 Ω	0.99 Ω	9.9 Ω	29.7 Ω	56.1 Ω
123.2	1.32 Ω	2.64 Ω	5.28 Ω	47.52 Ω	125.4 Ω	231 Ω
168.9	6.6 Ω	13.2 Ω	19.8 Ω	224.4 Ω	594 Ω	1320 Ω
202.3	19.8 Ω	36.3 Ω	69.3 Ω	726 Ω	1584 Ω	3498 Ω

Table II shows the dependence of voltage noise by the sampling rate while Table III shows the resistance resolution for 10 μA constant current depending on the sampling rate. To

calculate the resistance resolution, the peak-to-peak noise voltage was calculated first by multiplying the RMS noise voltage by 6.6 and then divided by 10 μA.

The best ratio of performance and speed of measurement was achieved by using 15 Hz sampling rate. From the Tables, at an input range of 25 mV and 15 Hz sampling rate, the peak–to-peak noise of the resistance, using 10 μA constant current, was only about 0.11 Ω. This design circuit with low noise can also support the measurement of resistance from many gas sensor elements up to 64 gas sensors.

B. MWCNTs/Polymer Composite Characterization

The pure dispersed MWCNTs and MWCNTs/polymer composites were investigated by using a scanning electron microscope (SEM) as displayed in Fig. 3 and 3b, respectively. Using chemical treatment, the MWCNTs were quite well dispersed in solvents (see Fig. 3a). The diameters of MWCNTs are within a range of 60-180 nm. After the deposition of the MWCNTs/polymer composites on the sensor element, SEM image (see Fig. 3b) showed the insertion of MWCNTs inside the hole of polymer. Creation of these nanochannels can be expected to enhance the surface-to-volume ratio and reactivity between gas molecule and sensing material [11,12] leading to an increase in the sensitivity of typical polymer gas sensor.

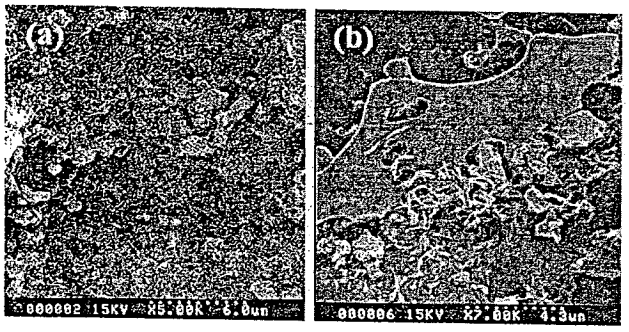

Fig. 3 SEM images of (a) pure dispersed MWCNTs and (b) MWCNTs/PS composite surfaces.

C. Indoor Air Monitoring

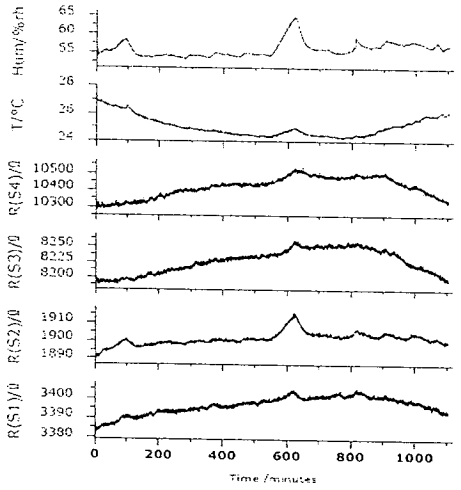

Fig. 4 Gas sensor signals from long time measurement in a room.

The sensor elements showed a highly selective sensitivity to acetic acid vapors but as good as no response to ethanol, methanol and water vapor. The long-term stability of the sensor elements was tested over a period of 18.5 hours in normal air in the laboratory. It can prove that this networked E-Nose based on MWCNTs/polymer composite gas sensor array can be used to monitor the environment with low noise (See Fig. 4).

Conclusion

The design and implementation of a networked E-nose has been presented for online detection of indoor air. The MWCNTs/polymer composite gas sensors as prepared by drop coating technique were used as a gas sensing array. The new designed constant current circuit was employed to measure the resistance of gas sensor array. The results showed the designed measurement circuit with very low noise (at sampling rate < 100 Hz, the relative noise < 0.02%) and insertion of MWCNTs inside the hole of polymer that can enhance the sensitivity of typical polymer gas sensor. It is hoped that this work will have many uses for new development of low cost networked E-nose system for indoor air monitoring.

Acknowledgments

This research was supported by Mahidol University and Kasetsart University. C.W. acknowledges TRF-CHE-KU Research Grant for New Scholar (MRG 5580229).

References

[1] K. Tikk, et al., Meat Science, Vol. 80, pp. 1254-1263, 2008.

[2] N. Barié, et al., Sens. Actuat. B, Vol. 114, pp. 482–488, 2006.

[3] C. Wongchoosuk, et al., *Mater. Res. Innovat.*, Vol. 13, pp. 185-188.

[4] P. Lorwongtragool et al., *Proceeding of ECTI-CON 2011*, pp. 163 – 166, 2011.

[5] R.E. Baby, et al., *Sens. Actuat. B*, Vol. 69, pp. 214–218, 2000.

[6] H. P. Chan, et al., *Lung Cancer*, Vol. 63, pp. 164–168, 2009.

[7] C. Wongchoosuk, et al., *Sensors*, Vol. 9, pp. 7234-7249, 2009.

[8] C. Wongchoosuk, et al., *Proceeding of DSR 2011*, pp. 1-4, 2011.

[9] R. Fend, et al., *J. Clin. Microbiol.* Vol. 44, pp 2039-2045, 2006.

[10] C. Wongchoosuk, et al., Malodor detection based on electronic nose, Chapter 3 in air quality monitoring, assessment and management, ISBN: 978-953-307-317-0, pp. 41-74, 2011.

[11] C. Wongchoosuk, et al., *Sens. Actuat. B*, Vol. 147, pp. 392-399, 2010.

[12] C. Wongchoosuk, et al., *Sensors*, Vol. 10, pp. 7705-7715, 2010.

Diabetes Diagnosis by Direct Measurement from Urine Odor Using Electronic Nose

Satetha Siyang
Materials science and Engineering Program
Faculty of Science, Mahidol University
Bangkok, Thailand
E-mail : S.satetha@gmail.com

Teerakiat Kerdcharoen*
Department of Physic and Center of Nanoscience and Nanotechnology, Faculty of Science, Mahidol University
Bangkok, Thailand
NANOTEC Center of Excellent at Mahidol University, National Nanotechnology Center, Thailand
Email : sctkc@mahidol.ac.th

Chatchawal Wongchoosuk*
Department of Physics
Faculty of Science, Kasetsart University
Bangkok, Thailand
E-mail : chatchawal.w@ku.ac.th

Abstract—**Diabetes is one of the most common chronic eases and can occur at any age. To avoid many side effects of betes on health, early detection of diabetes is very necessary. In ; paper, we propose an alternative method to detect diabetes ed on direct measurement of urine odor by using an electronic e (E-nose). Artificial urines, used to simulated a situation of betes patient, were produced by adding glucose into the pure ne samples. Eight commercial chemical gas sensors were used the sensing elements of our e-nose. Principal components ılysis (PCA) and cluster analysis (CA) methods were employed data analysis. The PCA and CA results show that the proposed hnique was able to identify the glucose concentration in urine. the future, e-nose can be a potential tool for diabetes diagnosis healthcare personnel as well as home users.**

Index Terms—**E-nose, PCA, smart toilet, chemical sensor, betes.**

I. INTRODUCTION

Diabetes is one of the most common chronic diseases sed by metabolic malfunction in carbohydrate metabolism. m the report of World Health Organization (WHO) based on gust 2011, there are 364 million diabetes patients in the ·ld and more than 80% of diabetes deaths occur in low-and ldle-income countries. In Thailand, the Bureau of Non nmunicable Disease reported that there were about 0.6 lion diabetes patients in 2010. The data shows that diabetes n important disease that can occur in every people.

Diabetes occurs either when the pancreas does not produce ıugh insulin or when the body cannot effectively use the ılin it produces. Insulin is a hormone that regulates blood cose levels. Hyperglycaemia is a common effect of ontrolled diabetes and over time leads to serious damage to ıy of the body's system, especially the nerves and blood vessels. The diabetes diagnosis can be made by measurement of cose level in blood. In general, there are three methods uding; (i) fasting plasma glucose test, (ii) oral glucose rance test, and (iii) random plasma glucose test for diabetes diagnosis. All of these methods can measure the level of glucose but their procedures are quite complicated and time-consuming. Another method for fast diabetes diagnosis is the measurement of glucose in urine by using urine reagent strips. This method is quick and convenient but suffers low accuracy.

Electronic nose (E-nose) technology has been widely used in food industry, agriculture, environment monitoring and medical applications [1-5]. For example, the E-nose system was used to detect and discriminate exhaled breath of hepatocellular carcinoma patients [6] and diagnosis of urinary tract infection. [7].

In this paper, we have studied the possibility for diabetes diagnosis by direct measurement of urine odor using a lab-made e-nose. In general, urine contains very little glucose and other composition as shown in Table I. People with abnormal high blood sugar often have glucose in their urine because of diabetes. The effect of high level sugar in urine can cause a sweet or fruity odor. Therefore, e-nose may be applied for diabetes diagnosis of the urine odor directly.

TABLE I. COMPOSITION OF NORMAL URINE

Item	Amount (%wt)
Water	95
Inorganic salt	1.91
Urea	1.81
Organic ammonium salt	0.70
Organic compounds	0.56
Glucose	0.02

a. Data from "Nasa Contractor Report" [8]

8-1-4673-4892-8/12/$31.00 ©2012 IEEE

II. EXPERIMENTAL DETAILS

Sample collection and Preparation

Urine samples were collected from normal people that ve normal level of glucose in urine. The samples were llected and measured the temperature and volume mediately. Next, the sample was tested with urine reagent ip to ensure the normal glucose level in urine. Various ncentrations of glucose (Glucolin, 99% of glucose) were ded into the pure urine samples in order to simulate the ificial urines of diabetes patients. Six different samples were oduced as summarized in Table II.

TABLE II. THE DEFINITION OF EACH SPECIMEN

Definition	Item
Sample 1	Pure Urine
Sample 2	Pure Urine + 100 mg/dl glucose
Sample 3	Pure Urine + 250 mg/dl glucose
Sample 4	Pure Urine + 500 mg/dl glucose
Sample 5	Pure Urine + 1000 mg/dl glucose
Sample 6	Pure Urine + 2000 mg/dl glucose

Urine reagent strips testing

The urine samples were tested by urine reagent strips for imating the concentration of glucose. Urine strip was npletely dipped into the sample and immediately removed avoid dissolving of the reagent areas, waiting for 30 onds. The color change of the reagent area was compared he corresponding color chart on the bottle label.

Measurement by the Electric Nose

After testing the sample with urine reagent strips, the nples were measured by an E-nose. The schematic diagram our lab-made e-nose system was shown in Fig. 1. The perature of the sample was controlled by thermostat and ied as follows: 35, 40, and 45°C.

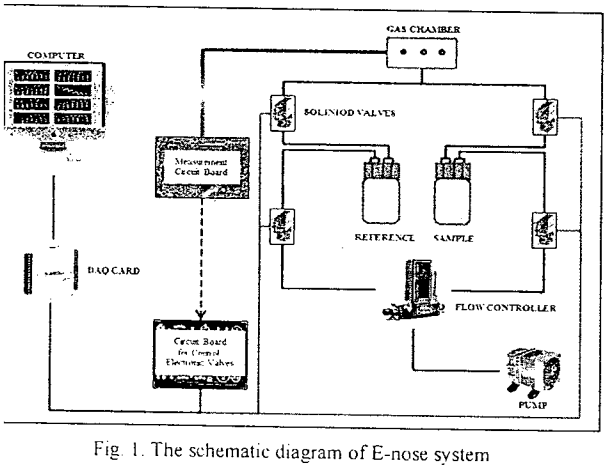

Fig. 1. The schematic diagram of E-nose system

III. RESULT AND DISCUSSION

A. Urine reagent strips testing

Based on adding of the amount of glucoses as summarized in Table II, the result of urine reagent strips testing is displayed in Fig. 2. The color of reagent area is in good agreement with the color chart of standard database. It indicates that artificial urine for diabetes patient can be simply produced by direct adding of glucose amounts summarized in Table II.

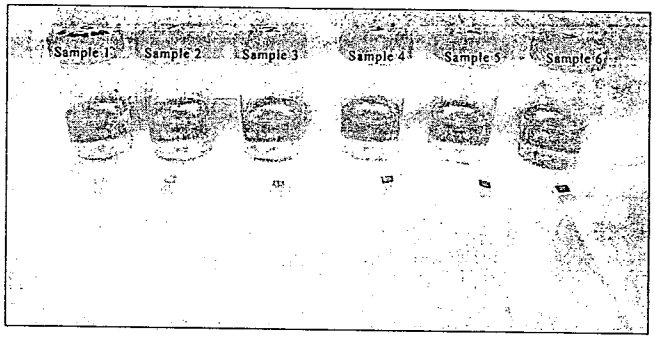

Fig. 2. Result of urine strip reagent testing

B. Sensor Response

The response of gas sensor (S_i) was calculated by the following equation;

$$S_i = | R_0 - R_s | / R_0 \qquad (1)$$

Where

R_0 is resistance of sensor in pure air

and R_s is resistance of sensor in sample odors

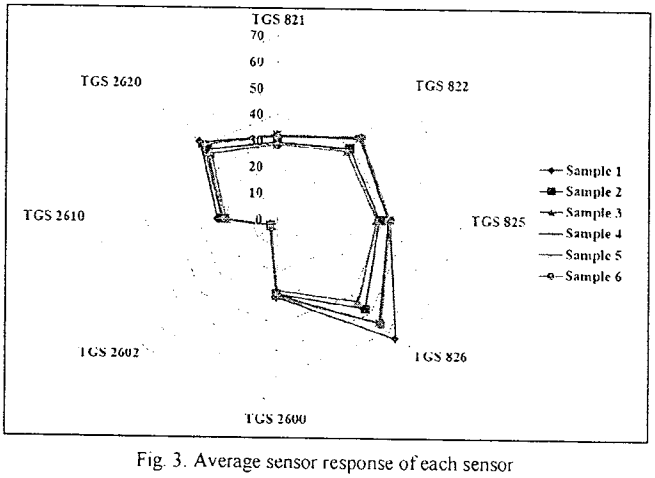

Fig. 3. Average sensor response of each sensor

The average sensor response was calculated and plotted against with the concentrations of glucose as shown in Fig. 3. The highest response of 65% is obtained from TGS 826 sensor while TGS 2602 sensor gives the lowest sensor response of 3% on sample 1.

From the datasheets of gas sensor (http://www.figaro sensor.com), TGS 826 is the sensor for ammonia detection. From the composition of urine as show in Table I, there is

7 wt% of organic ammonia salt in urine so this causes the gh sensor response of TGS 826. In case of TGS 2602, this nsor is generally used for detection of air contaminants such toluene and hydrogen sulfide. Such contaminants are not ajor composition of urine. Therefore, the TGS 2602 sensor ows the lowest sensor response. However, the TGS gas nsors were not designed to detect the fruity odor. The sensor sponses are not linear with the glucose concentration but ey can generate the unique patterns. Therefore, the data will introduced into principal components analysis (PCA) and ister analysis (CA) for further data analysis.

Principal Components Analysis (PCA)

To specify the level of glucose in urine, the principal nponents analysis (PCA) was used for pattern recognition. ine samples were measured by varying temperatures (35, 40, d 45°C). In principles, the increase of temperature has an ect to the evaporation rate of the solution that can cause tinct sensor response.

At temperature of 35°C, the result of PCA is not clearly parated in each concentration as shown in Figure 4 (a). When temperature increases to 40°C, there is a bit shift of sample 1 m other samples. Almost all samples are still grouped within same region. For the temperature at 45°C, the PCA result arly shows the separation of normal urine from other nples. There are two groups that can be noticed as shown in . 4 (c). The left side is low concentration of glucose and ht side is moderate and high concentrations of glucose.

Cluster Analysis (CA)

To study the distinction of PCA point in each experiment, cluster analysis method (CA) was used. The results are wn in Fig. 5. At the temperature of 35°C and 40°C, the CA ults scatter conformably to the PCA results. These peratures cannot identify the normal people that have mal level of glucose in urine. High order of CA result was erved when the temperature of measurement increases to C. There is two large groups. First group is sample 1 and ple 2. Second group is sample 3, 4, 5 and 6. For first group, e is a little similarity of PCA point. The result conforms to PCA results as shown in Fig 4 (c). For the second group, ple 5 can be clearly separated from the samples 3, 4 and 6. m cluster analysis, it can be concluded that the increase of perature during measurement can increase the possibility of tronic nose for diabetes diagnosis.

IV. CONCLUSION

The study of diabetes diagnosis by direct measurement n urine odor with electronic nose was achieved with ing the temperatures. The commercial TGS gas sensors e used as the sensing section and the highest sensitivity was erved from TGS 826 sensor that can detect gas ammonia. PCA and CA method were employed in data analysis.

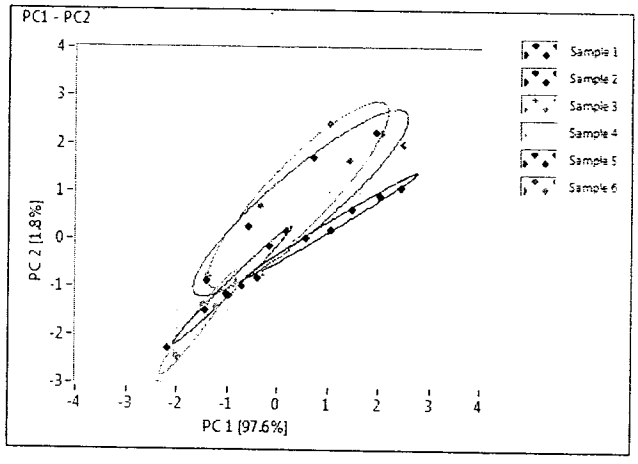

(a)

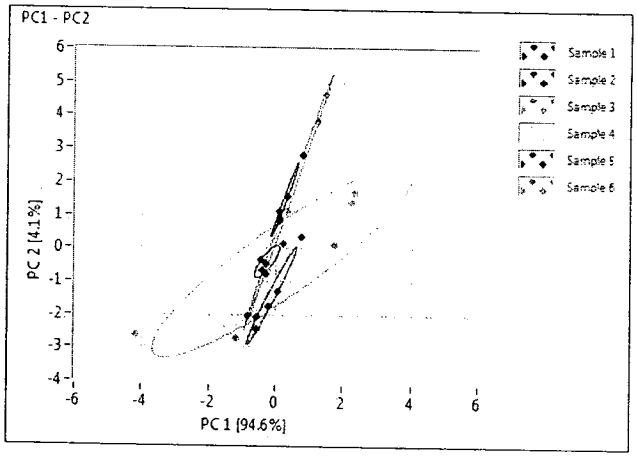

(b)

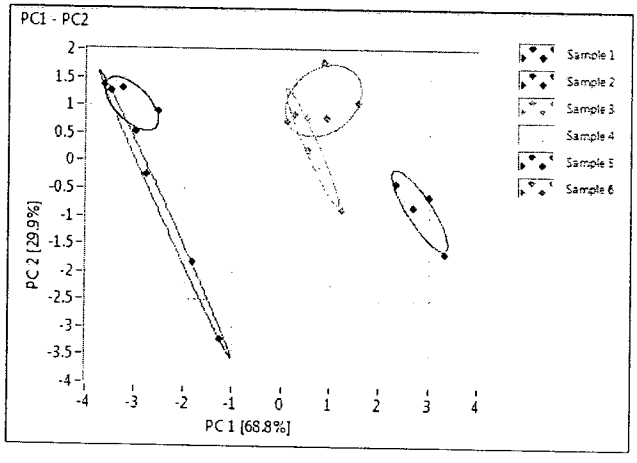

(c)

Fig. 4. Principal Components Analysis (PCA) of glucose in urine as various temperature (a) 35°C, (b) 40°C, and (c) 45°C

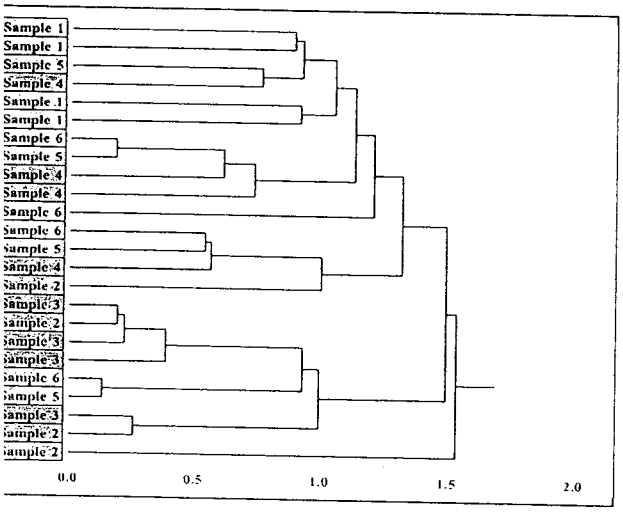

(a)

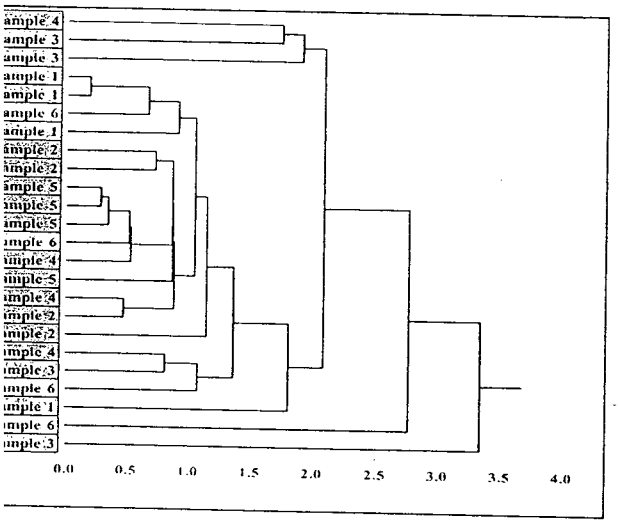

(b)

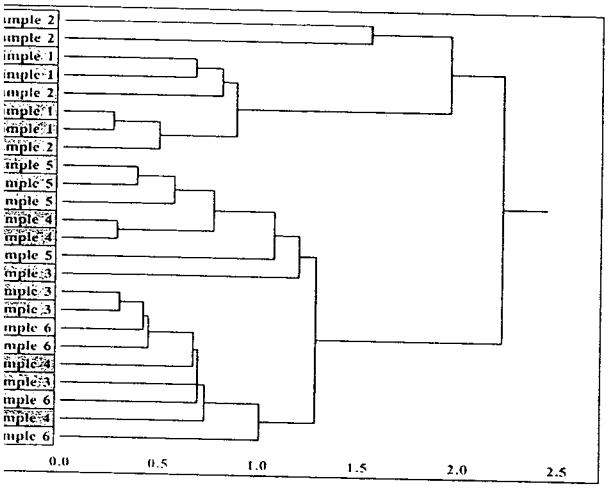

(c)

5. Cluster Analysis (CA) of glucose in urine as various temperatures (a) 35°C, (b) 40°C, and (c) 45°C

From the PCA and CA results, it was shown that the increment of sample temperature can increase the possibility for identification of the concentration of glucose in urine. Based on this preliminary study, our lab-made e-nose can be a potential device for diabetes diagnosis by direct measurement from urine odor with applied the temperature (>45 °C).

ACKNOWLEDGMENT

This research was supported by Mahidol University and National Nanotechnology Center (grant no. P-12-01157). C.W. acknowledges TRF-CHE-KU Research Grant for New Scholar (MRG 5580229).

REFERENCES

[1] S.Y. Yurish, "Sensor and transducers application", Sensors & Transducers Journal, vol. 107, pp. 17-25, August 2009.

[2] A.D. Wilson and M. Baietto, "Applications and advance in electronic-nose technologies", Sensor, June 2009

[3] A.D. Wilson and M. Baietto, "Advances in electronic-nose technologies developed for biomedical applications", Sensors, vol.11, pp. 1105-1176, January 2011.

[4] P.E. Keller, L.J. Kangas, L.H. Liden, S. Hashem, and R.T. Kouzes, "Electronic noses and their applications", October 1995.

[5] A. Perera, T. Pardo, T. Sundiae, R. Gutierrez-Osuna, S. Marco and J. Nicolas, "Electronic nose for remote bad odour monitoring system in landfill sites"

[6] T. Seesaart, C. Khunarak, T. Kerdcharoen, and T. Kitiyakara, "Development of an electronic nose for detection and discrimination of exhaled breath of hepatocellular carcinoma patients", Unpublished

[7] A.K. Pavlou, N. Magan, C. McNulty, J.M. Jones, D. Sharp, J. Brown, and A. P.F. Tuner, "Use of an electronic nose system for diagnoses of urinary tract infections", Biosensors and Bioelectronics, vol. 17, pp. 893-899, May 2002.

[8] C.D. Natale, A. Mantini, A. Macagnano, D. Antuzzi, R. Paolesse, and A.D. Amico, "Electronic nose analysis of urine samples containing blood", Physiol. Meas., vol. 20, pp. 377-384, September 1999.

[9] D.F. Putnam, "Composition and concentrative properties of human urine", Unpublished

[10] W. Ping, T. Yit, X. Haibao, and S. Farong, "A novel method for diabetes diagnosis based on electronic nose", Biosensors & Bioelectronics, vol.12, pp. 1031-1036, May 1997.

[11] C.D. Natale, R. Paolesse, A. Macagano, A. Mantini, A. D'Amico. A. Legin. L. Lvova, A. Rudnitskaya, and Y. Vlasov, "Electronic nose and electronic tongue integration for improved classification of clinical and food samples", Sensor and Actuators, vol. B64, pp. 15-21, 2000.

[12] M.A. Drake, P.D. Gerard, J.P. Kleinhenz, and W.J. Harper, "Application of an electronic nose to correlate with descriptive sensory analysis of added cheddar cheese", Lebensm.-Wiss. U.-Texhnol., vol.36, pp. 13-20, March 2002

[13] C. Apetrei, I.M. Apetrei, S. Villanueva, J.A. de Saja, F. Gutierrez-Rosales, and M.L. Rodriguez-Mendez, "Combination of an e-nose, and e-tounge and an e-eye for the characterization of olive oils with different degree of bitterness", Analytica Chimica Acta. vol. 663, pp. 91-97, January 2010.

Bread Baking Aroma Analysis by an Intelligent Electronic Nose System for Future Robotic Chef

K. Timsorn[1], C. Khunarak[2], P. Nipakul[1], T. Pogfay[3], and C. Wongchoosuk[1,*]

[1]*Department of Physics, Faculty of Science, Kasetsart University, Bangkok, 10900 Thailand*
[2]*Materials Science and Engineering Programme, Faculty of Science, Mahidol University, Bangkok, 10400 Thailand*
[3]*Nanoelectronics and MEMS Laboratory, National Electronics and Computer Technology Center, Klong Luang, Pathumthani, 12120 Thailand*
**Corresponding author. E-mail: Chatchawal.w@ku.ac.th*

Abstract

Electronic nose (E-nose) is an instrument that can be used to detect and distinguish volatile organic compounds (VOCs) with high accuracy and fast operating time. The E-nose can be applied to various fields such as food analysis, medicine, environmental control, and industrial processes. Combined with robot technologies (robotic chef), the E-nose may be installed and used to detect food aromas during cooking process. In this work, we have developed the E-nose for robotic chef noses. An example of application for robotic chef noses has been demonstrated in case of bread baking aromas detection. The bread baking process has been varied at four different baking temperatures of 40, 60, 80, and 100 °C and four different baking time of 5, 10, 15, and 20 minutes. The percentage changes of sensor resistance and principal component analysis (PCA) method have been employed to analyze the data. The results show that the E-nose can detect bread baking aromas and clearly classify the bread with baking process at different conditions. This study will be useful for robotic chef noses in various food quality applications in near future.

Keywords: E-nose, food quality control, PCA method, robotic chef

Introduction

Electronic nose (E-nose) is an olfactory sensing system that mimics mammalian nose for detection of volatile organic compounds (VOCs) [1]. Presently, E-nose systems have continually been developed to apply in different engineering and industrial areas including food quality analysis, medicine and environmental control etc. In case of food industries applications, the E-nose can be used for detecting the food spoilage [2], identifying the state of freshness [3,4] and monitoring the toxic contamination in beverage [5]. The performance of E-nose is directly related to the different responses of sensors [6]. One of the challenges for the practical food application of E-nose is to detect and distinguish food aromas during cooking processes. If this purpose can be done, the E-nose may be used as a sensing part in robotic chef.

In this work, we have constructed an E-nose and used for the detection of bread baking aromas at four different baking temperatures and four different baking times. Eight metal oxide semiconductor gas sensors were used as sensing part of the E-nose Percentage changes of sensor responses and principal component analysis (PCA) method have been employed to analyze the data.

Materials and Methods

Bread baking preparation

Fresh bread purchased from a market in Bangkok was baked at four different baking temperatures; 40, 60, 80 and 100 °C, and four different baking times; 5, 10, 15 and 20 minutes. Then, the baked bread was cut into samples with weight about 1-2 g. The samples were placed in the sample bottle for E-nose analysis.

E-nose system

The schematic diagram of E-nose system is shown in Fig. 1. It consists of three main components; (I) valves and air pump with mass flow controller,(II) sensor array, and (III) data acquisition (DAQ) & computer. For sensor array, the eight commercial Taguchi gas sensors (TGS) were used as sensing part as listed in Table 1.

Starting, a pump will suck clean air into a mass flow controller. The mass flow controller was used to control air flow rate. In this experiment, the air flow rate was set at 2 L/min. The solenoid valves were used to select the path of aroma molecule delivery. The zero air in the reference bottle was sucked into

sensor array chamber for 5 minutes in order to be a reference line and clear bread baking aromas in sensor chamber. When the sensor responses reached to the resistance baseline, valve 2 was closed and valve 3 was opened. Bread baking aromas in the sample bottle were sucked into sensor array for 1 minute. Then, the resistances of sensors were recorded every 1 minute as a function of time via DAQ for subsequent analysis.

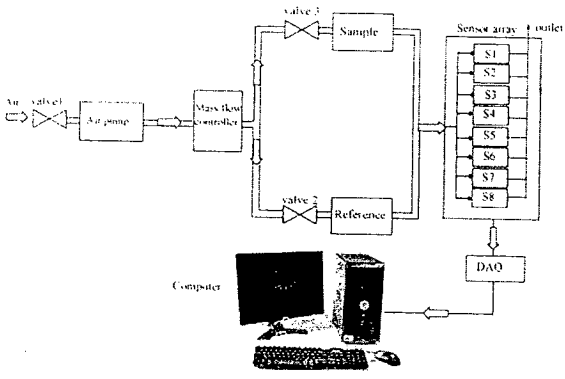

Figure 1. Schematic diagram of E-nose system.

Table 1: Lists of sensor array

Sensor number	Sensor name	Sensing type
S1	TGS 821	Hydrogen
S2	TGS 822	Organic Solvent Vapors
S3	TGS 825	Hydrogen Sulfide
S4	TGS 826	Ammonia
S5	TGS 2600	Air Contaminants
S6	TGS 2602	Air Contaminants
S7	TGS 2610	LP gas
S8	TGS 2620	Solvent Vapors

Principal component analysis (PCA)

The principal component analysis (PCA) [7,8] was employed for recognition and discrimination of bread baking aromas from measurements of the E-nose system. In principles, PCA process contains five following steps: (I) Get data from matrix, (II) Normalize the data matrix by the mean subtraction, (III) Calculate the covariance matrix, and determine eigenvectors and eigenvalues of the covariance matrix. The calculated eigenvectors must be unit eigenvectors. (IV) Rearrange the eigenvectors and eigenvalues. The eigenvectors are ordered by eigenvalues from highest to lowest. And (V) Obtain the PCA result by matrix multiplication and transpose. The obtained new dataset with orthogonal linear transformation are usually plotted in two or three dimensions containing the most relevant of the data set.

Results and Discussion

The resistance changes of each sensor are displayed in Fig. 2. We can be seen that these curves differ from each other in the form of curve shapes and maximum value of resistance changes depending on the type of each sensor. This result shows that all sensors are sensitive to bread baking aromas. The resistances of all sensors decrease when the bread baking aromas are introduced into sensor chamber. It implies that most deoxidizing gases can emit from the bread baking.

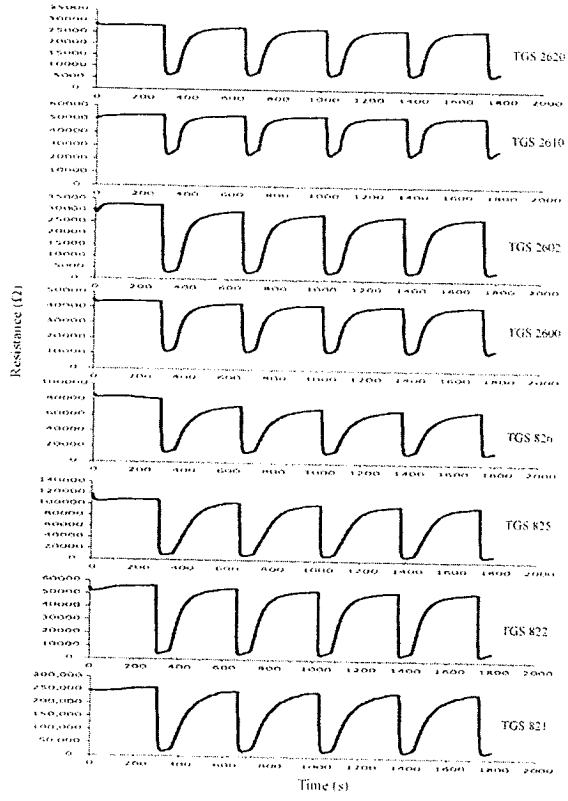

Figure 2. Resistance changes of each sensor as a function of time.

The percentages of sensor responses can be obtained from following equation;

$$\text{Sensor reponse (\%)} = \frac{R_0 - R_{Sens}}{R_0} \times 100 \qquad (1)$$

where R_0 is the value of resistance baseline and R_{Sens} is the value of sensitive resistance.

Fig. 3 shows the three dimensional plot of the percentages of sensor responses at different baking temperatures for baking time of 15 min. We can obviously observe that all sensors exhibit high response to the bread baking aromas in the range of

60-95% at all baking temperatures. At baking temperature of 60 °C, all sensors show the highest response. It refers that more VOCs can emits at this temperature. If baking temperature is so high, some VOCs can be lost.

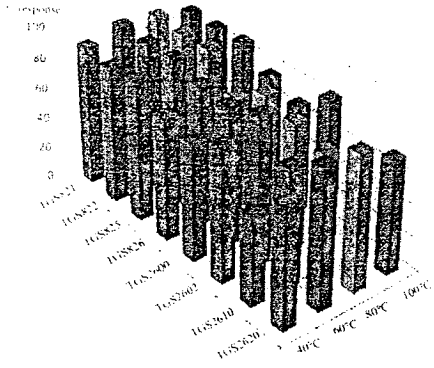

Figure 3. 3D plot of the percentages of sensor response at different baking temperatures.

All data sets were introduced into PCA. Fig. 4 shows the PCA plot of bread baking aromas at different baking temperatures. It can be observed that the PCA plot clearly discriminates the bread baking aromas to four clusters related to different baking temperatures and time. The best result occurs at baking time of 15 min. From results, it suggests that baking time of 15 min can well generate the unique pattern of bread baking aromas at a function of baking temperatures.

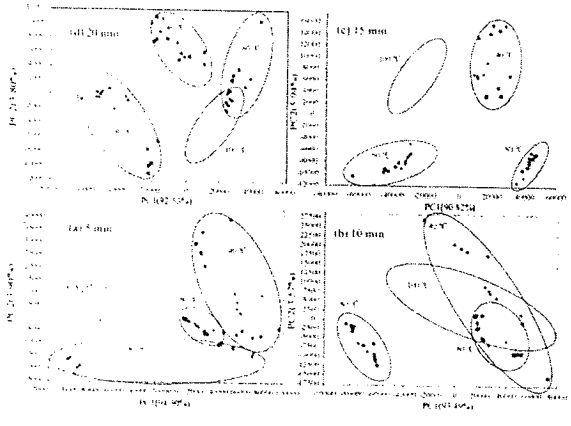

Figure 4. PCA plot of bread baking aromas at (a) 5 min, (b) 10 min, (c) 15 min, and (d) 20 min of baking time with different baking temperatures.

Conclusions

In this work, an E-nose has been developed for food application during cooking processes. An example has been demonstrated in term of bread baking aromas detection and classification. The TGS sensor array shows high response to bread baking aromas in the range of 60-95%. With condition of bread baking time at 15 min and baking temperature of 60 °C, the bread product can generate a unique pattern of aroma. Combined with PCA method, our E-nose can classify bread baking aromas at the different bread baking conditions. It is hoped that our E-nose will be installed in robotic chef for real-time monitoring food aroma during cooking processes in near future.

Acknowledgments

Preproposal Research Fund (PRF) from Faculty of Science, Kasetsart University and TRF-CHE-KU Research Grant for New Scholar (MRG 5580229) are gratefully acknowledged for supports of this research.

References

1. S. Sankaran, L. R. Khot and S. Panigrahi, "Biology and Application of Olfactory Sensing System: A Review", Sensors and Actuators B: Chemical **171-172** (2012) 1-17.
2. I.A. Casalinuovo, D. D. Pierro, M. Coletta and P. D. Francesco, "Application of Electronic Noses for Disease Diagnosis and Food Spoilage Detection", Sensors **6** (2006) 1428-1439.
3. N. E. Barbri, A. Amari, M. Vinaixa, B. Bouchikhi, X. Correig, E. Llobet, "Building of a metal oxide gas sensor-based electronic nose to assess the freshness of sardines under cold storage", Sensors and Actuators B: Chemical **128** (2007) 235–244.
4. H. Guohua, W. Yuling, Y. Dandan, D. Wenwen, Z. Linshan and W. Lvye, "Study of Peach Fressness Predictive Method Based on Electronic Nose", Food Control **28** (2012) 25-32.
5. C. Wongchoosuk, A. Wisitsoraat, A. Tuantranont, T. Kerdcharoen, "Portable electronic nose based on carbon nanotube-SnO_2 gas sensors and its application for detection of methanol contamination in whiskeys, Sensors and Actuators B: Chemical 147 (2010) 392-399.
6. A. Ponzoni, A. Depari, M. Falasconi, E. Comini, A. Flammini, D. Marioli, A. Taroni and G. Sberveg, "Bread Baking Aromas Detection by Low-Cost Electronic Nose", Sensors and Actuators B **130** (2008) 100-104.
7. H. Yu, J. Wang, H. Xiao and M. Liu, "Quality Grade Identification of Green Tea Using The Eigen Values of PCA Based on The E-Nose Signals", Sensors and Actuators B **140** (2009) 378-382.
8. S. Capone, M. Epifani, F. Quaranta, P. Siciliano, A. Taurino and L. Vasanelli, "Monitoring of Rancidity of Milk by Means of An Electronic Nose and A Dynamic PCA Analysis", Sensors and Actuators B **78** (2001) 174-179.

AACCS 2013

CHIANG MAI, THAILAND

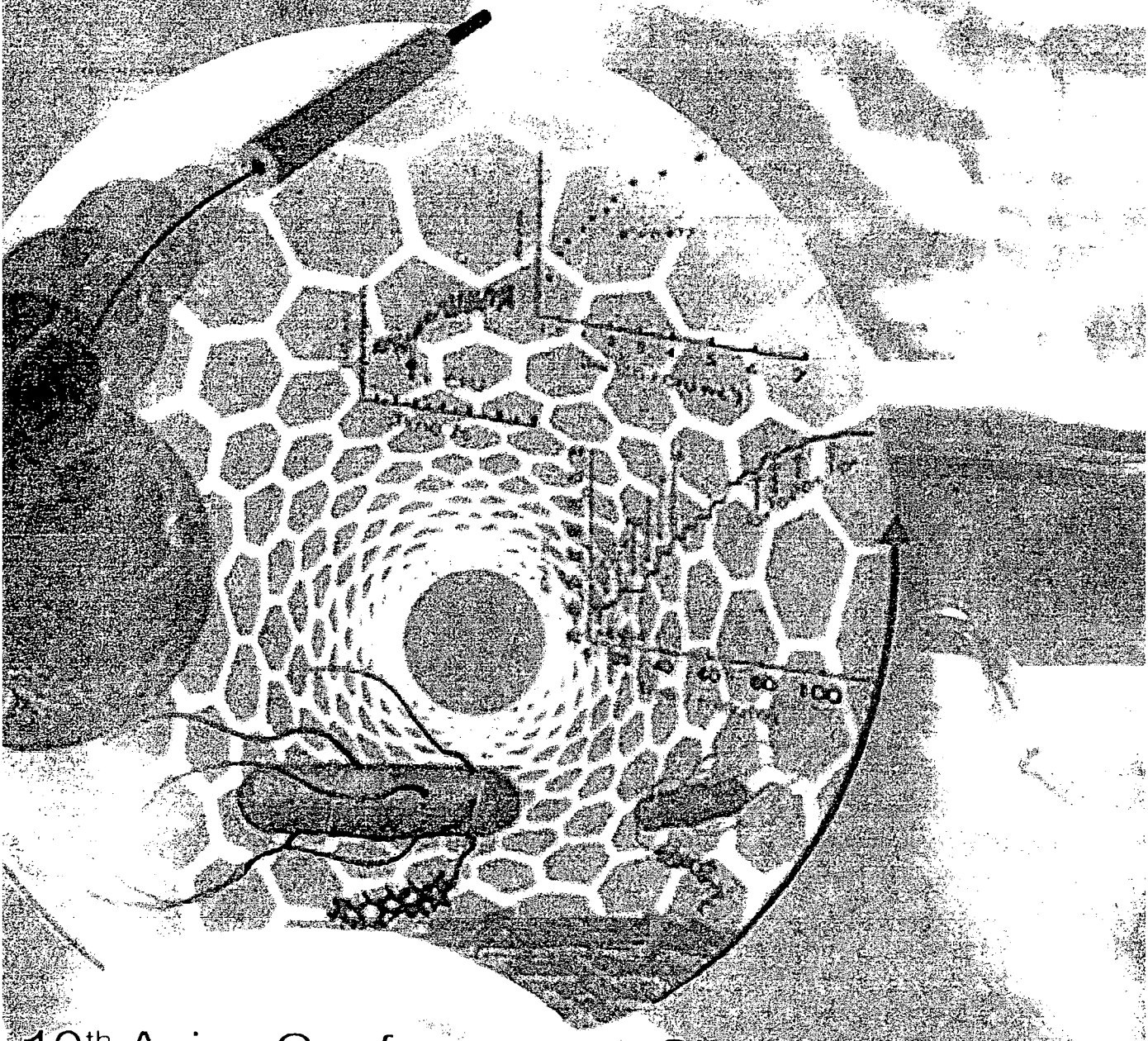

10th Asian Conference on Chemical Sensors

Chemical Sensors for the Sustainable Society

11-14 NOVEMBER 2013 @ THE EMPRESS HOTEL, CHIANG MAI, THAILAND

사단법인 한국센서학회
THE KOREAN SENSORS SOCIETY
Seoul, Korea

NECTEC
a member of NSTDA

HERP - NRU

MR CENTER

Faculty of Science Chiang Mai University

B2-007

Invention of Stereo Electronic Nose for Mobile Robot

Yotsarayuth Seekaew[1], Wasu Klanritt[1], Sittipong Promchaem[1], and Chatchawal Wongchoosuk[1,*]

[1]*Department of Physics, Faculty of Science, Kasetsart University, Bangkok 10900, Thailand*
* *Corresponding author. E-mail:* chatchawal.w@ku.ac.th

Although human olfactory system is able to discriminate more than 10,000 different odorants, detection of chemicals with high molecular weight (>300 daltons) and various toxic gases are still limited. Nowadays, the gas-sensitive mobile system has become a necessary tool to detect toxic gas and gas leaks in several situations since many gases can highly affect people's health and they are difficult to detect by human nose. In this paper, we have described a design of gas-sensitive system (called as stereo electronic nose) that is suitable for installing on a mobile robot. The stereo electronic nose system consists of four gas sensors including methane CNG gas sensor (MQ-4), LPG gas sensor (MQ-6), flammable gas sensor (MQ-9), and air quality control gas sensor (MQ-135). Such gas sensors were installed at a center of rectangular box. Two fans were set up at sidewalls of box with controllable of the air flow direction by using an electric relay circuit. The stereo electronic nose system has tasted in closed chamber with several gases. The distance between gas sources and stereo electronic nose has been varied from 5-80 cm with many directions in order to investigate the relative equations for identification of the gas leak source. The results show that the stereo E-nose can sense a various types of gases and can identify the direction of gas sources. The gas sensitivity of stereo E-nose decreases when source distance increases. Our stereo E-nose can be used as the olfactory system in a mobile robot for gas source identification.

Keywords: Electronic nose, Metal oxide, Semi-conductor gas sensors, Gas source identification

References

1. Wongchoosuk, C.; Wisitsoraat, A.; Phokharatkul, D.; Horprathum, M.; Tuantranont, A.; Kerdcharoen, T. Sens. Actuators B, **2013**, 181, 388-394.
2. Ishida, H.; Nakayama, G.; Takamichi ; Moriizumi, T. *IEEE Sens. J.*, **2005**, 5, 537-545.
3. George, F.F.; Leon, M.C.; Afonja, A.; Binions, R. *Sensors*, **2010**, 10, 5469-5502.
4. El Barbri, N.; Llobet, E.; El Bari, N.; Correig, X.; Bouchikhi, N. *Sensors*, **2008**, 8, 142-156